*J. Fluid Mech.* (1999), *vol.* 389, *pp.* 303–334. Printed in the United Kingdom



# Saline and particle-driven interfacial intrusions

By FRANS DE ROOIJ, P. F. LINDEN† AND STUART B. DALZIEL

Department of Applied Mathematics and Theoretical Physics, University of Cambridge, Silver Street, Cambridge CB3 9EW, UK
e-mail: f.derooij@damtp.cam.ac.uk

(Received 9 February 1998 and in revised form 30 November 1998)

This paper presents a theoretical and experimental investigation into saline and particle-driven intrusions along the interface between two layers of different densities. The conditions at the nose of an intrusion are described in an analysis similar to that applied by Benjamin (1968) to boundary gravity currents. Equations for propagation velocity and front position as functions of relative density are derived. These are used in an integral model for intrusions, which also includes the effects of sedimentation of particles and detrainment of interstitial fluid. The model describes the time-evolution of the length of the intrusion and the sediment distribution it produces. Laboratory experiments were carried out with lock-releases of a fixed volume of saline or particle-laden fluid into a two-layer stratification. Measurements were taken of the intrusion propagation, intrusion position and sediment distribution, and are found to be in good agreement with the solutions of the integral model.

## 1. Introduction

Horizontal density gradients in a fluid may give rise to gravity currents, sometimes called density currents. The density gradients can be due to differences in fluid composition, phase, temperature or concentration of suspended particulate. In a sufficiently quiescent environment a sharp front may be formed across which a density difference exists between the current and the surroundings. This density difference drives the mainly horizontal motion of the gravity current. When the surrounding fluid is vertically stratified, the gravity current can enter it at intermediate levels where its density is comparable with that of the ambient, and is then called a gravity intrusion.

Gravity intrusions occur frequently in the atmosphere, when rising buoyant air reaches levels where its density matches the ambient density and spreads out horizontally. A striking example is the outflow above volcanic plumes which carry ash high into the atmosphere and then spread laterally over many thousands of kilometres. Gravity intrusions are also an important phenomenon in oceanography. A much-quoted example is the warm but saline outflow from the Mediterranean in the eastern Atlantic ocean which produces a saline intrusion at about 1000 m depth. Particle-driven intrusions in the ocean can occur when material is suspended by a river outflow, by an underwater landslide from a shelf edge, or even artificially

† Present address: Department of Applied Mechanics and Engineering Sciences, University of California, San Diego, 9500 Gilman Drive, La Jolla, CA 92093-0411, USA.

by dredging machines in the routes to seaports. The gravity current thus produced (termed a turbidity current by oceanographers) runs along the bottom of the ocean down to a level where it has the same bulk density as the surrounding fluid at which point it may lift off to form an intrusion. Gravity intrusions are also thought to play an important role in the flow in sedimentation tanks of sewage treatment plants. The sewage with a high concentration of dense suspended material enters the tank, and relatively light sediment-free fluid flows out at the top of the tank. In steady flow conditions, a vertical particle concentration gradient is set up with a corresponding continuous density stratification. With varying inflow conditions, gravity intrusions can occur, possibly inducing an unwanted increase of the particle concentration of the outflow.

Much of the work on these topics stems from an analytical description of gravity currents running along a rigid boundary published in 1968 by Benjamin, and a large number of publications on gravity currents has appeared since. A comprehensive overview of gravity currents is provided in the book by Simpson (1997). Holyer & Huppert (1980) extended Benjamin's analysis to gravity intrusions along the density interface in a two-layer fluid. Laboratory experiments on gravity intrusions and on the interfacial waves and bores that intrusions can produce in layered stratifications have been published respectively by Britter & Simpson (1981) and Rottman & Simpson (1989).

Bonnecaze and co-workers (1993, 1995) describe studies of particle-driven gravity currents caused by an increased bulk density due to suspended material. They describe numerical solutions of the shallow water equations modified to account for the reduction in the density of a particle-driven gravity current due to the settling of the particles. Their solutions for planar and axisymmetric flows agree well with the results of their laboratory experiments. Dade & Huppert (1995) made the comparison with earlier oceanographic data of deposition from gravity currents. On the basis of their earlier models Bonnecaze, Huppert & Lister (1996) proposed an algebraic equation to predict the thickness of the layer of sediment, or deposit, left behind by a particle-driven gravity current. An equation for the sedimentation from polydisperse currents was obtained by superposition of the sedimentation of the different fall velocities.

Rimoldi, Alexander & Morris (1996) carried out laboratory experiments on particle-driven intrusions running from a shelf edge bottom topography into a two-layer fluid. They offered a phenomenological description of the flow, as well as quantitative measurements of the sediment. However, no theory was presented to explain their results. Maxworthy (1999) reports experiments on sedimenting gravity currents along a free surface, which were seen to produce a dense particle-laden underflow. The modelling of this flow is in an early stage.

The present work is an investigation of both saline and particle-driven gravity intrusions along the density interface in a two-layer fluid contained in a rectangular channel. The vertical position of the intrusion, the propagation speed and particle deposition are looked at in detail. In § 2, a theoretical description of intrusions along a density interface is given. From this description convenient equations for depth and speed of intrusions of arbitrary density are derived. A leading-order theory for sedimenting particles is presented, which is consequently used in an integral model for intrusions, leading to predictions for propagation speed and the distribution of deposited sediment. The experimental apparatus used is described in § 3, and § 4 describes the results of the experiments. The measurements of the speed and the deposition are compared with the analytical results. Finally, § 5 provides the conclusions and an outline of future work.

## 2. Theoretical modelling

### 2.1. *Nose conditions*

One way to create a two-dimensional gravity current in a channel is with a so-called lock-release in a rectangular tank. The released fluid has a finite, fixed volume per unit channel width $A = x_0 h_0$, where $x_0$ is the length of the lock and $h_0$ the initial height of the lock-release. In the following analysis, we assume the lock contains dense fluid and thus generates a bottom gravity current, but similar arguments apply to a light surface gravity current. The evolution of these gravity currents is known to go through several phases.

In the first phase, known as the slumping phase, the fluid escapes from the lock. The nose of the current has a constant height and propagates at a constant speed. A rarefaction wave, or hydraulic jump, propagates to the back of the lock, reflects and propagates as a bore towards the nose of the current. Experiments have shown (Simpson 1997) that it catches up with the nose at a distance of approximately $10x_0$ from the lock. At this point, the information that the length of the lock was finite has reached the nose and a second phase, in which the flow is self-similar, begins. Basic continuity ensures the current retains a constant total buoyancy while the continued propagation requires the height of the current to decrease as its length increases. The propagating current slows down; its length now increasing as $t^{2/3}$, as shown by Huppert & Simpson (1980). Subsequently, as the gravity current becomes thinner and slower, a third phase is attained when viscous effects become important. In this third phase the current spreads as $t^{1/5}$. On a free surface, a final phase may be observed, where surface tension and viscous forces determine the flow.

Gravity intrusions follow a similar evolution as they propagate away from a finite-volume release. We shall restrict our attention, however, to only the first two phases. During these phases the flow is governed by a balance between inertial and buoyancy forces. The spreading velocity of the current is characterized by the conditions at the nose: the height $h$ and the reduced gravity $g' = g\Delta\rho/\rho$ are of prime importance. The analysis of an interfacial intrusion will proceed along similar lines to those set out by Benjamin (1968) for a boundary current.

*Energy-conserving intrusion*

Consider an intrusion of density $\rho_1$ flowing into a two-layer fluid, consisting of an upper layer with depth $H_0$ and density $\rho_0$ over a lower layer with depth $H_2$ and density $\rho_2$, as sketched in figure 1. Mixing, viscosity and surface tension are assumed to be absent. We choose a frame of reference in which the intrusion is at rest. In this frame, the ambient fluid far upstream has a horizontal velocity $U$, and far downstream the velocities are $V_0$ and $V_2$ above and below the intrusion, respectively. The origin of the vertical coordinate $z$ is chosen at the level of the interface far upstream. The intrusion has a vertical extent from $-h_2$ to $h_0$.

The pressure is defined to be zero at the stagnation point $S$ at the nose of the intrusion. This point has an elevation $\zeta$ above the upstream interface. Following the analysis of Holyer & Huppert (1980), Bernoulli's equation can be applied along the interface ahead of the intrusion in the two layers of fluid to yield

$$\left.\begin{aligned} \rho_0 g\zeta &= p_A + \tfrac{1}{2}\rho_0 U^2, \\ \rho_2 g\zeta &= p_A + \tfrac{1}{2}\rho_2 U^2. \end{aligned}\right\} \tag{1}$$

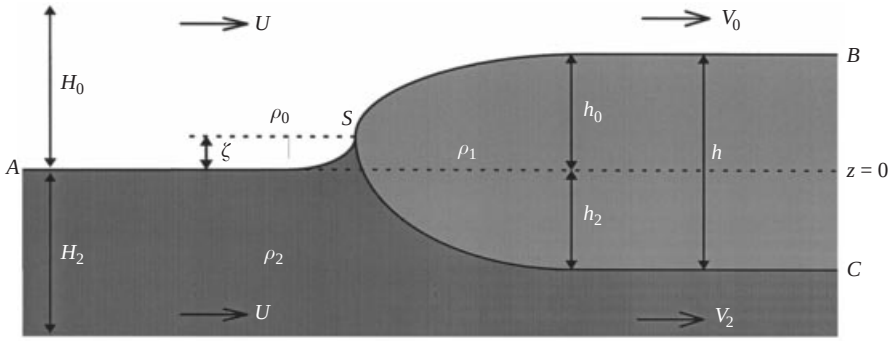


FIGURE 1. Sketch of an intrusion along the interface between two shallow layers, in the frame of reference of the intrusion.

Since $\rho_0 \neq \rho_2$, (1) implies $p_A = 0$ and also that

$$\zeta = \frac{U^2}{2g}. \tag{2}$$

This shows that the nose of an intrusion always has to be slightly lifted above the interface to balance the dynamic pressure and to give a continuous pressure across the upstream interface.

To simplify the treatment of the pressure field, we subtract the vertical hydrostatic pressure variation, which has different gradients in the two layers of ambient fluid. For the upstream pressure, this yields $p_U = 0$ everywhere. For the downstream pressure field $p_D(z)$, we assume that the fluid within the intrusion is stationary, hence the pressure is zero on the level of the stagnation point at the nose, and we express $p_D$ in terms of the reduced gravities $g'_{01} = g(\rho_1 - \rho_0)/\rho_0$ and $g'_{12} = g(\rho_2 - \rho_1)/\rho_2$. These upstream and downstream pressure fields can be used to write down Bernoulli's equation for a streamline just above the intrusion between points $S$ and $B$, and for a streamline just below the intrusion between points $S$ and $C$:

$$0 = \tfrac{1}{2}\rho_0 V_0^2 - \rho_0 g'_{01}(h_0 - \zeta), \tag{3}$$

$$0 = \tfrac{1}{2}\rho_2 V_2^2 - \rho_2 g'_{12}(h_2 + \zeta). \tag{4}$$

These equations only hold for a non-dissipative intrusion, where the top and bottom interfaces of the intrusion are streamlines. Mass conservation in both layers of ambient fluid gives

$$H_0 U = (H_0 - h_0)V_0, \tag{5}$$

$$H_2 U = (H_2 - h_2)V_2. \tag{6}$$

Finally, conservation of flow force over the entire flow yields

$$\begin{aligned} H_0\rho_0 U^2 + H_2\rho_2 U^2 = {} & (H_0 - h_0)\rho_0 V_0^2 + (H_2 - h_2)\rho_2 V_2^2 + (H_2 - h_2)(-g'_{12}\rho_2 h_2) \\ & + \int_{-h_2}^{0} (g'_{12}\rho_2 z)\mathrm{d}z + \int_{0}^{h_0} (-g'_{01}\rho_0 z)\mathrm{d}z + (H_0 - h_0)(-g'_{01}\rho_0 h_0) \\ & + (H_0 + H_2)g\rho_1\zeta. \end{aligned} \tag{7}$$

Assuming that $H_0, H_2, \rho_0, \rho_1$, and $\rho_2$ are given, we now have the six equations, (2)–(7),

for the six unknowns $U$, $V_0$, $V_2$, $h_0$, $h_2$ and $\zeta$. Unfortunately, these equations cannot be solved analytically for arbitrary values of the densities and layer depths. An equivalent set of equations, but with slightly different definitions, was solved numerically by Holyer & Huppert (1980). They found that the solution was not unique for a range of fluid depths and densities. By applying the criterion of maximum volume inflow rate, they obtained numerical solutions for the relative depths of energy-conserving intrusions over the continuous range of densities and layer depths.

Despite the lack of an analytical solution, manipulation of the above system of equations offers some additional insight. We proceed by combining Bernoulli's equation (3) and the mass conservation equation (5) for the upper layer, yielding after substitution of $\zeta$ from (2)

$$\tfrac{1}{2}U^2\left\{\frac{H_0^2}{(H_0-h_0)^2}+\frac{g'_{01}}{g}\right\}=g'_{01}h_0. \tag{8}$$

The first term in the brackets is at least of order unity, whereas for intrusions where only small relative density differences occur, the second term is much smaller than unity and can be neglected in the further analysis.

Since the same arguments can be applied to the lower layer, this gives two expressions for the propagation speed of the intrusion:

$$U=\sqrt{2g'_{01}h_0}\left(1-\frac{h_0}{H_0}\right), \tag{9}$$

$$U=\sqrt{2g'_{12}h_2}\left(1-\frac{h_2}{H_2}\right). \tag{10}$$

Of course, these two velocities have to be the same. In the simplified case of a symmetrical intrusion, with $H_0=H_2$ and $g'_{01}=g'_{12}$, this means that $h_0=h_2$. Based on Benjamin's statement that only a boundary current of half-depth can be energy-conserving, we expect an intrusion of half-depth in both layers ($H_0=2h_0, H_2=2h_2$) to be a solution of these equations. Substitution shows that it indeed satisfies the equations (2) and (3)–(7). The propagation speed for this symmetric half-depth intrusion is

$$U=\frac{1}{\sqrt{2}}\sqrt{g'_{01}h_0}=\frac{1}{\sqrt{2}}\sqrt{g'_{12}h_2}, \tag{11}$$

identical to the propagation velocity of an energy conserving boundary current in shallow surroundings. Indeed, apart from the slightly raised nose, the flow is symmetrical around the upstream interface and equivalent to two single-layer currents into shallow surroundings.

*Intrusion in two infinitely deep layers*

A useful approximation for an intrusion entering two deep layers of fluid ($H_0$, $H_2 \gg 1$) can be obtained by applying an analysis similar to Benjamin's analysis of a boundary current in an infinitely deep ambient. The upstream and downstream velocity profiles are assumed to be smooth and the vertical pressure variation is therefore hydrostatic everywhere far away from the nose.

Choose a point $E$ far downstream within the intrusion at the same level as the nose stagnation point $S$, so that $z_E=\zeta$ and $p_E=p_S=0$. Comparing the pressure between point $E$ and point $A$ on the upstream interface via circuits through the upper and

lower layers yields

$$\left.\begin{aligned} p_E - p_A &= gh_0(\rho_1 - \rho_0) - g\rho_1\zeta, \\ p_E - p_A &= gh_2(\rho_2 - \rho_1) - g\rho_1\zeta. \end{aligned}\right\} \tag{12}$$

Since the application of Bernoulli's equation along the upstream interface showed that $p_A = 0$, these pressure differences have to be zero. Substituting $\zeta$ from (2) yields two equations for the propagation speed $U$ of the intrusion. Equating these gives equations for the height of the intrusion in the two layers as a function of the reduced gravities (that now have a slightly different definition, with a $\rho_1$ in their denominator), expressed as fractions of the total depth of the intrusion $h = h_0 + h_2$:

$$h_0 = \frac{g'_{12}}{g'_{01} + g'_{12}} h = (\tfrac{1}{2} - \varepsilon)h, \tag{13}$$

$$h_2 = \frac{g'_{01}}{g'_{01} + g'_{12}} h = (\tfrac{1}{2} + \varepsilon)h, \tag{14}$$

where the second part of these equations provides convenient expressions for the heights in terms of the parameter $\varepsilon$, characterizing the relative density of the intrusion. It is defined as

$$\varepsilon = \frac{\rho_1 - \overline{\rho}}{\Delta\rho}, \tag{15}$$

where $\overline{\rho} = \frac{1}{2}(\rho_0 + \rho_2)$ is the average density of the two layers and $\Delta\rho = \rho_2 - \rho_0$ the density difference between the two layers. The value of $\varepsilon$ ranges from $-0.5$ for an intrusion density equal to the light top layer, to 0.5 for an intrusion of density equal to the dense lower layer. Equations (13) and (14) show that the intrusion will mainly flow into the layer with which it has the smallest density difference: a light intrusion will be raised with respect to the upstream interface, a dense intrusion will sink.

The propagation speed of the intrusion can be expressed as

$$U = \sqrt{2}\sqrt{\frac{g'_{01}g'_{12}}{g'_{01} + g'_{12}} h} = \sqrt{2}\sqrt{\tfrac{1}{2}g'_{02}}\sqrt{\tfrac{1}{2}h}\sqrt{1 - 4\varepsilon^2}. \tag{16}$$

For a symmetrical intrusion of average density ($\varepsilon = 0$), the speed is maximal, and matches with (9) in the limit $H \to \infty$. Both halves of the flow are identical to a boundary gravity current. An intrusion with a density different from the mean density of the two layers ($\varepsilon \neq 0$) will have a lower propagation speed than a symmetrical intrusion. We use the propagation speed $U_{sym}$ of this symmetrical intrusion to define the Froude number as

$$Fr = \frac{U_{sym}}{\sqrt{\tfrac{1}{4}g'_{02}h}}. \tag{17}$$

Equation (16) shows that $Fr = \sqrt{2}$ for an intrusion between two infinitely deep layers.

*Intrusion with energy losses*

Holyer & Huppert (1980) also examined flows where energy losses occur. Introducing head losses $\Delta\eta_0$ and $\Delta\eta_2$ for the upper and lower layers (respectively) they obtained numerical solutions for the energy losses. In a stability analysis, they showed that waves can occur on the downstream interfaces of the intrusion, and their wavelengths and amplitudes were calculated.

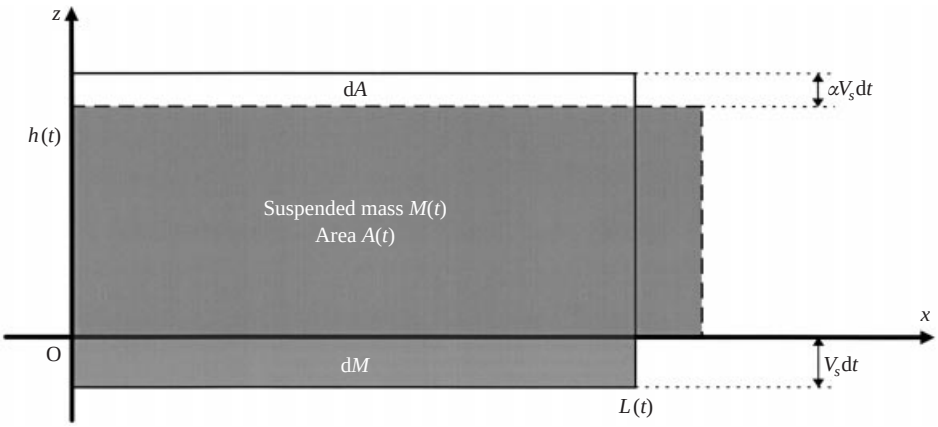


FIGURE 2. Definitions for the integral model for a boundary gravity current.

We will take a different approach and try to put the solutions for dissipative and non-dissipative flow into one equation. For a symmetric intrusion ($\varepsilon = 0$), the only difference between the velocity $U$ given by (11) (non-dissipative intrusion in shallow ambient) and (16) (intrusion in infinitely deep ambient) is a different value of the multiplicative factor, the Froude number. It seems reasonable, therefore, to expect the dependence on $\varepsilon$ of the intrusion velocity in infinitely deep surroundings, given in (16), to be valid for shallow surroundings too, and hence

$$U = Fr\sqrt{\tfrac{1}{4}g'_{02}h}\,\sqrt{1-4\,\varepsilon^2}, \tag{18}$$

for intrusions in arbitrarily deep surroundings. Although it has not turned out to be possible to show this analytically for asymmetric intrusions in arbitrary surrounding fluid depth, we have confidence that this dependence will hold and experiments, reported below, support this hypothesis.

*Effects of a finite interface thickness*

So far, we have looked at the theoretical case of an infinitely thin interface between the two layers. Britter & Simpson (1981) have reported on experiments investigating the effects of a finite interface thickness. For interface thicknesses $\delta$ up to one-fifth of the intrusion depth $h$, they found that the head of the intrusion resembles a boundary current reflected in the interface and the Froude number remains unchanged. For larger interface thicknesses, however, the characteristic breaking billows behind the head are reduced in magnitude. The intrusion propagates more slowly, giving a 20% lower Froude number for a relative interface thickness $\delta/h = 0.8$, as shown in figure 2 of their paper. In this paper we concentrate on cases with sharp interfaces. However, as we shall see in the discussion of figure 14 in §4, it proved difficult to attain an effectively sharp interface in the experiments, and the effects of a finite interface thickness have to be taken into account.

### 2.2. *Integral models*

Insight can also be gained from a simple, integral model where the intrusion is represented by a rectangular region with a length $L(t)$ and a height $h(t)$, yielding a volume per unit channel width $A = Lh$, as depicted in figure 2. Any horizontal or vertical variations within the intrusion of velocity $U$ or fluid properties, represented

by the bulk reduced gravity $g'_{01}$, are ignored. For a saline intrusion one can then follow the analysis of Huppert & Simpson (1980) for boundary currents to obtain the aforementioned spreading law $L \sim t^{2/3}$, although here the use of the intrusion velocity (18) yields a different proportionality constant.

For a particle-driven intrusion, the relative density parameter $\varepsilon$ in (18) varies as a function of time owing to the sedimentation of particles, and the problem is more complicated. The assumptions described above imply that we assume the total suspended particulate mass $M$ to be well-mixed throughout the intrusion, although particles settle out through the bottom interface of the intrusion. The volumetric concentration $\phi$ can be expressed as

$$\phi = \frac{M}{Aw\rho_p}, \tag{19}$$

where $w$ represents the width of the channel. For an intrusion consisting of interstitial fluid of density $\rho_i$ and particles of density $\rho_p$, the bulk density of the intrusion is

$$\rho_1 = \rho_i + \phi(\rho_p - \rho_i), \tag{20}$$

which is used to calculate the bulk reduced gravity of the intrusion $g'_{10} = g(\rho_1 - \rho_0)/\rho_0$. In the analysis presented below we focus on entirely particle-driven intrusions, where the interstitial fluid $\rho_i$ does not contribute to the buoyancy driving the intrusion, and therefore set $\rho_i = \rho_0$.

At the bottom interface of the intrusion, the particles are assumed to settle out of the intrusion at a vertical velocity equal to the Stokes settling velocity $V_s$, which is valid for small-particle Reynolds numbers. The Stokes settling velocity is calculated by balancing the drag force with the buoyancy force that a body experiences owing to the density difference with the ambient fluid, which yields for a spherical particle with diameter $d$

$$V_s = \frac{g'_p d^2}{18v}. \tag{21}$$

Here $g'_p = g(\rho_p - \rho_0)/\rho_0$ represents the reduced gravity of the particle in the surrounding fluid and $v$ represents the kinematic viscosity of the fluid. This settling process is assumed to occur in a thin layer close to the interface where the vertical component of the turbulent velocity field is reduced by the presence of the density step. This sedimentation assumption gives a differential equation for the suspended mass

$$\mathrm{d}M = -\frac{M}{A} L V_s \mathrm{d}t. \tag{22}$$

As shown in figure 2, we also allow a fraction of the interstitial fluid to be detrained from the top of the intrusion. We assume that the detrainment is proportional to the sedimentation, and therefore obeys a differential equation similar to that for the particle sedimentation (22). We then have

$$\mathrm{d}A = -\alpha L V_s \mathrm{d}t \tag{23}$$

for the volume of the intrusion per unit width, where the value of the proportionality constant $\alpha$ will have to be determined form experimental observations. For negative values of $\alpha$ the intrusion entrains ambient fluid, whereas for $\alpha = 0$ the intrusion has a constant volume. Positive values of $\alpha$ indicate net detrainment of interstitial fluid, with the detrainment equalling the sedimentation at $\alpha = 1$ to yield an intrusion with a constant volumetric concentration of the particles. Here, interstitial fluid is being

regarded as detrained from the intrusion when it is depleted of particles and thus no longer contributes to the driving buoyancy force.

To obtain a differential equation for the intrusion length $L$ we use (18) for the propagation speed. That equation shows a dependence of the velocity on the relative density parameter $\varepsilon$, which, for a particle-driven intrusion, depends on the concentration of suspended material $\phi$. This can be expressed by substituting the bulk intrusion density (20) into the definition of $\varepsilon$ (15), giving

$$\varepsilon = -\tfrac{1}{2} + \phi\frac{\rho_p - \rho_0}{\rho_2 - \rho_0} = -\tfrac{1}{2} + (\varepsilon_0 + \tfrac{1}{2})\frac{\phi}{\phi_0}. \tag{24}$$

The constant $\varepsilon_0$ parameterizes the initial relative density of the intrusion containing particles at a concentration $\phi_0$. Substituting (24) into (18) we obtain

$$\mathrm{d}L = Fr\sqrt{g'_{02}h}\sqrt{(\varepsilon_0 + \tfrac{1}{2})\frac{\phi}{\phi_0}\left(1 - (\varepsilon_0 + \tfrac{1}{2})\frac{\phi}{\phi_0}\right)}\,\mathrm{d}t. \tag{25}$$

Equations (22), (23) and (25) can be expressed as a system of three coupled differential equations in the variables $M(t), A(t)$ and $L(t)$ by substituting $h = A/L$ and $\phi$ from (19). One approach to non-dimensionalizing this system would be to introduce a virtual source in which the density of the intrusion is equal to that of the lower layer, such that $\varepsilon = 0.5$ at some time $t = -\tilde{t}$. Such a virtual source would be short and tall, but match the actual release conditions at some later time $t = 0$. This would simplify the equations and replace the initial relative density ratio $\varepsilon_0$ with $\tilde{t}$ as a parameter in the solution. However, this approach cannot be used to recover all possible sets of initial conditions. In particular, for very light intrusions, insufficient sedimentation can occur in the period required for the length to increase from $L = 0$ to the actual source length $L_0$.

To enable us to consider the full range of possible initial conditions we non-dimensionalize the system of equations by scaling the variables with their values at the actual source $M_0, A_0$ and $L_0$ according to $M^* = M/M_0$, $A^* = A/A_0$ and $L^* = L/L_0$. Time is non-dimensionalized as $t^* = t/\tau_v$, where $\tau_v$ is the timescale for the propagation of the intrusion based on the ambient stratification:

$$\tau_v = \frac{L_0}{\sqrt{g'_{02}h_i}}, \tag{26}$$

where $h_i$ denotes the initial total intrusion thickness. We then have

$$\mathrm{d}M^* = -\frac{L^*M^*}{A^*}\frac{\tau_v}{\tau_s}\mathrm{d}t^*, \tag{27}$$

$$\mathrm{d}A^* = -\alpha L^*\frac{\tau_v}{\tau_s}\mathrm{d}t^*, \tag{28}$$

$$\mathrm{d}L^* = Fr\left(\frac{M^*}{L^*}\right)^{1/2}\left(\varepsilon_0 + \tfrac{1}{2} - (\varepsilon_0 + \tfrac{1}{2})^2\frac{M^*}{A^*}\right)^{1/2}\mathrm{d}t^*. \tag{29}$$

Here we have introduced a timescale $\tau_s$ for the settling of particles according to

$$\tau_s = \frac{A_0}{V_sL_0} = \frac{h_i}{V_s}. \tag{30}$$

In the further analysis we omit the stars that denote the dimensionless variables. The

initial conditions for the new non-dimensionalized variables are

$$M = A = L = 1 \quad \text{at } t = 0. \tag{31}$$

We proceed by integrating the ratio of (27) and (28) to give

$$A = M^{\alpha}. \tag{32}$$

This allows us to eliminate $A$ from the system to obtain

$$M^{\alpha-1}\mathrm{d}M = -\frac{\tau_v}{\tau_s}L\mathrm{d}t, \tag{33}$$

$$M^{\alpha-\frac{1}{2}}\left(\varepsilon_0 + \tfrac{1}{2} - (\varepsilon_0 + \tfrac{1}{2})^2 M^{1-\alpha}\right)^{1/2}\mathrm{d}M = -\frac{\tau_v}{\tau_s Fr}L^{3/2}\mathrm{d}L. \tag{34}$$

This equation can only be solved analytically for specific values of the detrainment parameter $\alpha$, yielding relationships between $L$ and $M$. Writing $k = \varepsilon_0 + \frac{1}{2}$ for convenience, these relationships become:

$$\sqrt{kM(1-kM)} + \sin^{-1}\sqrt{kM} - \sqrt{k(1-k)} - \sin^{-1}\sqrt{k} = -\frac{2\tau_v}{5\tau_s Fr}(L^{5/2}-1) \quad (\alpha = 0), \tag{35}$$

$$-\frac{8}{9k^2}[(k-k^2M^{3/4})^{3/2} - (k-k^2)^{3/2}] = -\frac{2\tau_v}{5\tau_s Fr}(L^{5/2}-1) \quad (\alpha = 1/4), \tag{36}$$

$$\sqrt{k-k^2M^{1/2}}\left(\frac{12Mk^2 - 4\sqrt{Mk} - 8}{15k^2}\right) - \sqrt{k-k^2}\left(\frac{12k^2-4k-8}{15k^2}\right) = -\frac{2\tau_v}{5\tau_s Fr}(L^{5/2}-1) \quad (\alpha = 1/2), \tag{37}$$

$$\tfrac{2}{3}\sqrt{k-k^2}(M^{3/2}-1) = -\frac{2\tau_v}{5\tau_s Fr}(L^{5/2}-1) \quad (\alpha = 1). \tag{38}$$

There are more analytical solutions of (34) for some rational values of $\alpha$ in the range $\frac{1}{2} < \alpha < 1$, but these have not been investigated. The solutions to (34) yield an explicit expression for $M(L)$ only for $\alpha = 1$ and $\alpha = \frac{1}{4}$, which, upon substitution in (29), yields a differential equation that can be solved numerically to give $L(t)$. The other cases yield an explicit expression for $L(M)$, although this may still be used to calculate a numerical solution for $L(t)$. Here, we will first analyse the solutions $L(t)$ for different values of the two experimental parameters, the relative initial density $\varepsilon_0$ and the ratio of the settling timescale to the propagation timescale $\tau_s/\tau_v$. Following this, we examine the effects of changes in the values of the modelling parameters, the detrainment parameter $\alpha$ and the Froude number $Fr$.

Figure 3 shows the numerical solution for several values of $\varepsilon_0$ (i.e. several values of the initial bulk density of the intrusion) with no detrainment ($\alpha = 0$). The symmetrical intrusion, with $\varepsilon_0 = 0$, has the highest initial propagation speed, as expected from (18). The initially denser intrusions, with larger values of $\varepsilon_0$ (e.g. $\varepsilon_0 = 0.4$), start with a lower velocity but accelerate to reach a maximum velocity when they have become centred on the interface (and $\varepsilon = 0$) owing to the sedimentation of particles. Further sedimentation then causes them to slow down as $\varepsilon$ becomes negative. The initially lighter intrusions (e.g. $\varepsilon_0 = -0.4$) remain above the interface and their velocity decreases monotonically from the start as the intrusion becomes lighter ($\varepsilon$ more negative) as the particles fall.

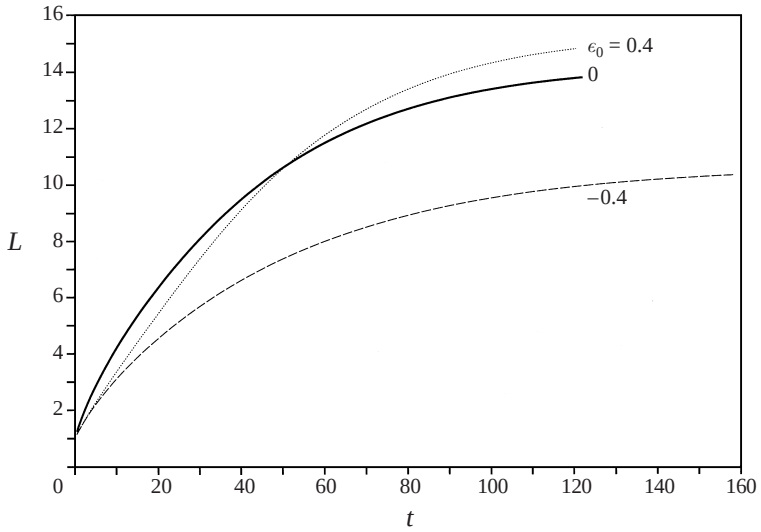


FIGURE 3. Solutions for a purely particle-driven interfacial intrusion length versus time, for different values of the initial relative density parameter $\varepsilon_0\tau_v/\tau_s = 0.0042$ to match the experimental conditions. Model parameters: detrainment parameter $\alpha = 0$, Froude number $Fr = 1$.

At later times, the interfacial intrusions reach a final length $L_f$, where they have lost all their suspended sediment and the driving buoyancy force no longer exists ($\varepsilon = -0.5$). Expressions for $L_f$ can be obtained easily from (35)–(38) by setting $M = 0$, which gives

$$L_f = \left\{1 + \frac{5\tau_s Fr}{2\tau_v}\left[\sqrt{\tfrac{1}{4} - \varepsilon_0^2} + \sin^{-1}\sqrt{\varepsilon_0 + \tfrac{1}{2}}\right]\right\}^{2/5} \quad (\alpha = 0), \tag{39}$$

$$L_f = \left\{1 + \frac{20\tau_s Fr}{9\tau_v}\left[\frac{(\varepsilon_0 + \frac{1}{2})^{2/3} - (\frac{1}{4} - \varepsilon_0^2)^{2/3}}{(\varepsilon_0 + \frac{1}{2})^2}\right]\right\}^{2/5} \quad (\alpha = \tfrac{1}{4}), \tag{40}$$

$$L_f = \left\{1 + \frac{5\tau_s Fr}{2\tau_v}\left[\frac{8\sqrt{\varepsilon_0 + \frac{1}{2}} + \sqrt{\frac{1}{4} - \varepsilon_0^2}\,(12\varepsilon_0^2 + 8\varepsilon_0 - 7)}{15(\varepsilon_0 + \frac{1}{2})^2}\right]\right\}^{2/5} \quad (\alpha = \tfrac{1}{2}), \tag{41}$$

$$L_f = \left\{1 + \frac{5\tau_s Fr}{3\tau_v}\sqrt{\tfrac{1}{4} - \varepsilon_0^2}\right\}^{2/5} \quad (\alpha = 1). \tag{42}$$

These final intrusion lengths are plotted in figure 4. The curve for $\alpha = 0$ shows that light intrusions have a shorter final length than dense intrusions, owing to their lower particle load. The effects of different values of $\alpha$ will be discussed later.

Figure 5(*a*) shows the time-evolution of interfacial intrusions with different ratios of the settling time to the propagation time $\tau_s/\tau_v$. The curves shown are for intrusions with identical relative initial densities, and their initial propagation velocity is seen to be independent of the ratio $\tau_s/\tau_v$. One can also show that the initial evolution of $L$ is independent of $\tau_s/\tau_v$ by integrating (27), (28) and (29) for $L \approx M \approx A \approx 1$, which

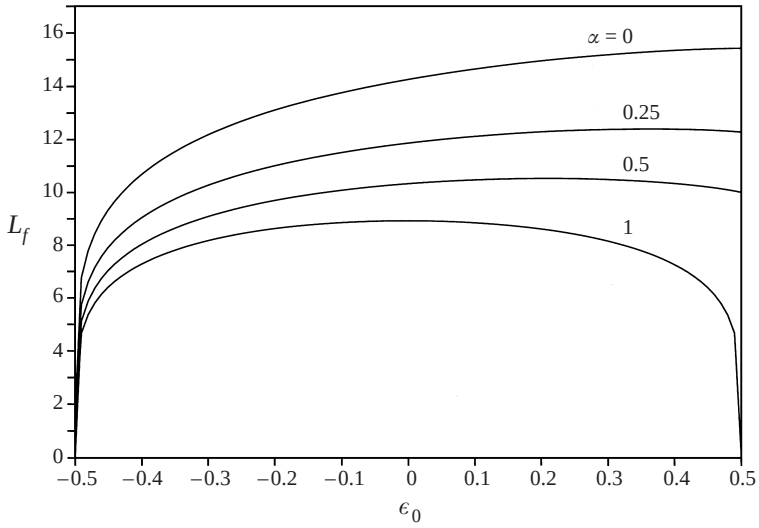


FIGURE 4. Final length of interfacial particle-driven intrusion, as a function of the relative initial density $\varepsilon_0$, for several detrainment parameter values $\alpha$. $\tau_v/\tau_s = 0.0042, Fr = 1$.

yields for $t \ll 1$

$$\left.\begin{aligned} M &= 1 - \tau_v t/\tau_s + O(t^2), \\ A &= 1 - \alpha\tau_v t/\tau_s + O(t^2), \\ L &= 1 + Fr\sqrt{\tfrac{1}{4} - \varepsilon_0^2}\,t + O(t^2). \end{aligned}\right\} \tag{43}$$

At later times, the curves deviate and the final lengths differ. Intrusions with a large ratio $\tau_s/\tau_v$ contain particles that settle relatively quickly, and run out of suspended material providing the driving force sooner. Intrusions with small values of $\tau_s/\tau_v$ propagate further. This behaviour can also be deduced from the final length given in (39).

The influence of the detrainment parameter $\alpha$ is investigated in figure 5($b$). Plotted curves are the solutions for $\alpha = 0, \frac{1}{2}$ and 1 for otherwise identical intrusions. We observe that at short times the propagation speed of the intrusion is almost independent of $\alpha$. A physical explanation for this can be given as follows. In obtaining (12), we vertically integrated the density profile in the intrusion to determine the buoyancy force. Any entrainment or detrainment will change the depth and density of the intrusion, but the integrated buoyancy force remains the same, which yields an unchanged propagation velocity. The final length that the intrusion reaches, however, does vary with $\alpha$. Figure 4 shows that higher values of $\alpha$ give a shorter final length: the detrainment of interstitial fluid increases the concentration $\phi$ in the intrusion, which enhances the sedimentation rate and thereby shortens the lifetime of the intrusion.

Finally, we look at changes in the time-evolution of the intrusion with the Froude number $Fr$. As stated before, the Froude number has been shown experimentally to

FIGURE 5. Interfacial particle-driven intrusion length as a function of time, for ($a$) different values of the ratio of the propagation time and the settling time $\tau_v/\tau_s$ ($\varepsilon_0 = 0, \alpha = 0, Fr = 1$); ($b$) different values of the entrainment parameter $\alpha$ ($\varepsilon_0 = 0.4, \tau_v/\tau_s = 0.0042, Fr = 1$); and ($c$) different Froude numbers $Fr$ ($\varepsilon_0 = 0, \tau_v/\tau_s = 0.0042, \alpha = 0$).

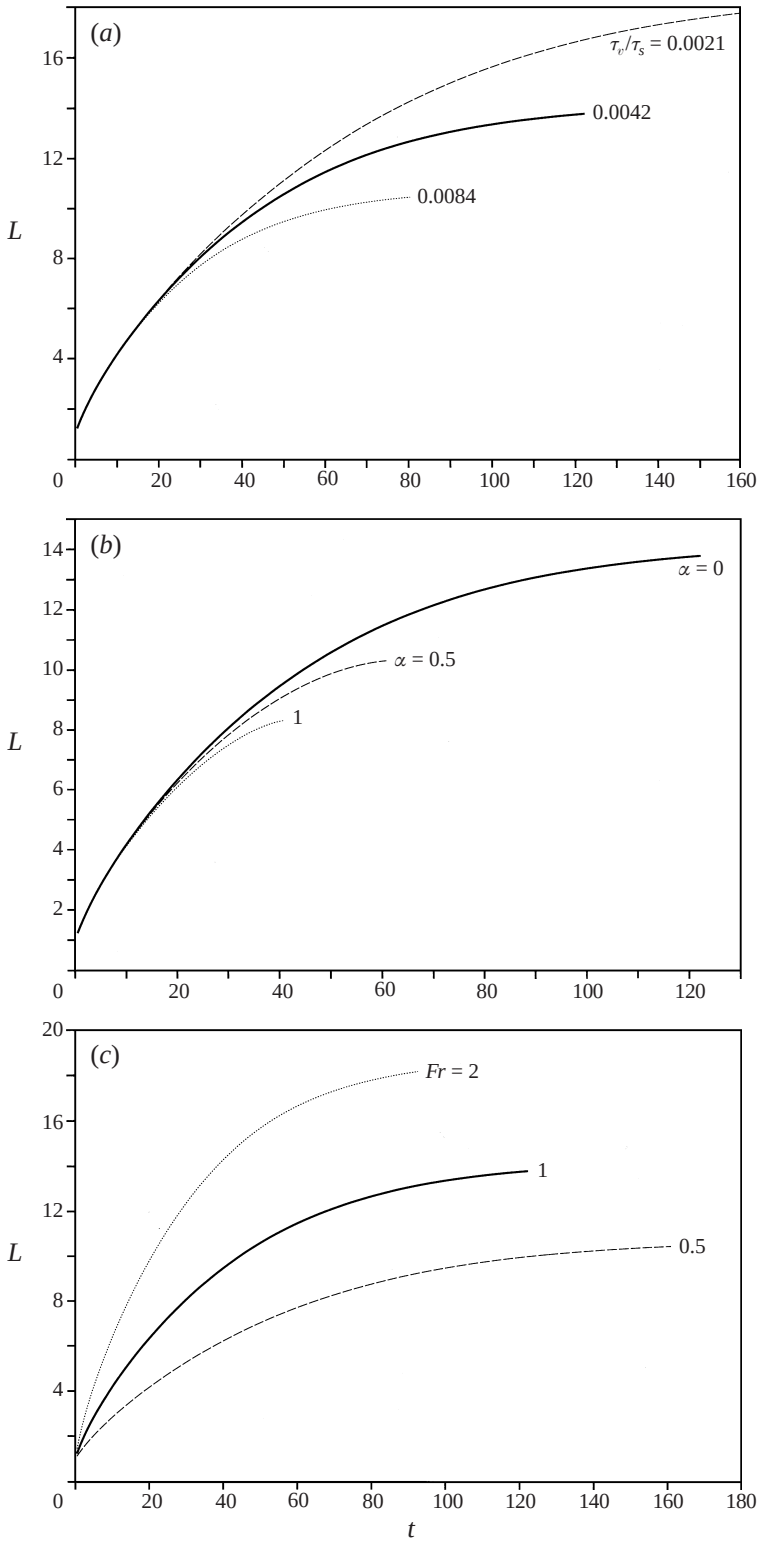


FIGURE 5. For caption see facing page.

depend on the ambient fluid depth and the thickness of the interface. Figure 5(*c*) shows that an increased Froude number yields a higher propagation velocity and a longer final intrusion length.

*Sediment deposition*

The final distribution of sediment from the intrusion can be computed from the solution for the amount of suspended material $M$ as a function of the intrusion length $L$, as given by (35), (37) and (38). Since we assumed that particles sediment homogeneously over the whole length of the intrusion, we calculate the thickness of the deposit $D(x)$ at every point outside the lock ($x > 1$, or, in dimensional form, $x > L_0$) by integrating the sedimentation from the time the intrusion reaches that point to the time when the intrusion has run out of sediment:

$$D(x) = -\int_{t_x}^{\infty} \frac{\mathrm{d}M}{\mathrm{d}t}\frac{1}{L}\mathrm{d}t = -\int_{x}^{L_f} \frac{\mathrm{d}M}{\mathrm{d}L}\frac{1}{L}\mathrm{d}t. \tag{44}$$

The deposit thickness everywhere in the lock ($0 < x < 1$) is identical to the thickness at the front of the lock ($x = 1$). Numerical integration yields deposition curves for different values of ($\varepsilon_0$), shown in figure 6(*a*). We notice that an initially light intrusion ($\varepsilon_0 < 0$) spreads its sediment over a shorter length than the symmetrical ($\varepsilon_0 = 0$) and the dense ($\varepsilon_0 > 0$) intrusion. The small difference in final lengths for symmetrical and dense intrusions displayed in figure 4 explains why their sediment distribution curves are also very similar.

Figure 6(*b*) shows how the sediment distribution varies with $\alpha$. The detrainment at larger values of $\alpha$ enhances the sedimentation rate and the extent of the deposit is smaller than for intrusions with no detrainment of interstitial fluid.

*Intrusion with constant nose thickness*

As we shall see in § 4, the assumption of a decreasing nose height for a propagating intrusion does not always match the experimental observations accurately. Using our integral model, we also investigated how a constant thickness of the nose would affect the propagation and the deposit distribution of the intrusion. We keep the sedimentation equation for $M$ (27) and the detrainment/entrainment relation for $A$ (28) unchanged. In the equation for the propagation velocity of the nose we now assume a constant nose height $h_0$, independent of the intrusion length $L$, which results in replacing (29) with

$$\mathrm{d}L^* = Fr\left(\frac{M^*}{A^*}\right)^{1/2}\left(k - k^2\frac{M^*}{A^*}\right)^{1/2}\mathrm{d}t^*. \tag{45}$$

Strictly speaking, this is inconsistent with the integral model assumption underlying the differential equations for $M$ and $A$. Nevertheless, we will seek to solve these equations since they could provide useful insight. We still envisage the intrusion as a rectangular box with no variation in thickness or particle concentration along its length, apart from a raised thickness at the very tip which only affects the propagation velocity.

Analogously to the derivation above, the equations can be integrated to obtain numerical solutions for the time-evolution of the length $L(t)$ and for the final spatial sediment distribution $D(x)$. These results for the intrusion length are plotted in figure 7. The straight lines are the solutions with $\alpha = 1$, corresponding to a detrainment of interstitial fluid equal to the sedimentation of suspended particles. In this case, the

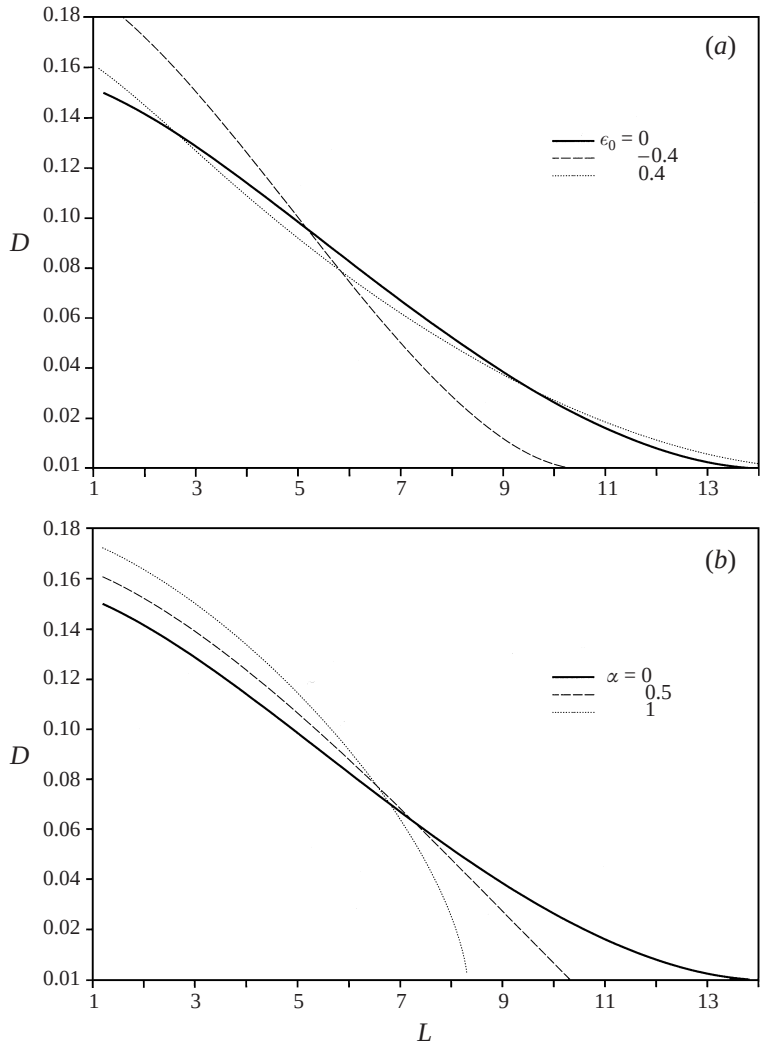


FIGURE 6. Solutions for the final sediment distribution of a particle-driven interfacial intrusion with $\tau_v/\tau_s = 0.0042$ and $Fr = 1$, at (*a*) different values of $\varepsilon_0(\alpha = 0)$, and (*b*) different values of $\alpha(\varepsilon_0 = 0)$.

concentration in the intrusion remains constant, which, combined with the constant nose height that we assumed, leads to the constant propagation velocity. The highest propagation velocity occurs at $\varepsilon_0 = 0$. Intrusions with $\varepsilon_0 = -0.4$ and $\varepsilon_0 = 0.4$ have the same, lower propagation velocity, a result of the symmetry around $\varepsilon_0 = 0$ of the velocity prediction by (18).

The curves that deviate from the straight lines in figure 7 are the solutions with $\alpha = 0$, corresponding to no detrainment of interstitial fluid. In this case, the concentration reduces owing to sedimentation and the propagation of the intrusion slows down with time. The symmetric intrusion ($\varepsilon_0 = 0$) has the largest initial propagation speed, but the initially dense intrusion ($\varepsilon_0 = 0.4$) reaches the furthest. This behaviour was also seen for the varying propagation speed integral model described above.

Figure 8 shows the numerical solutions for the deposit distribution from an interfacial intrusion with a constant nose height, and no detrainment ($\alpha = 0$). These curves

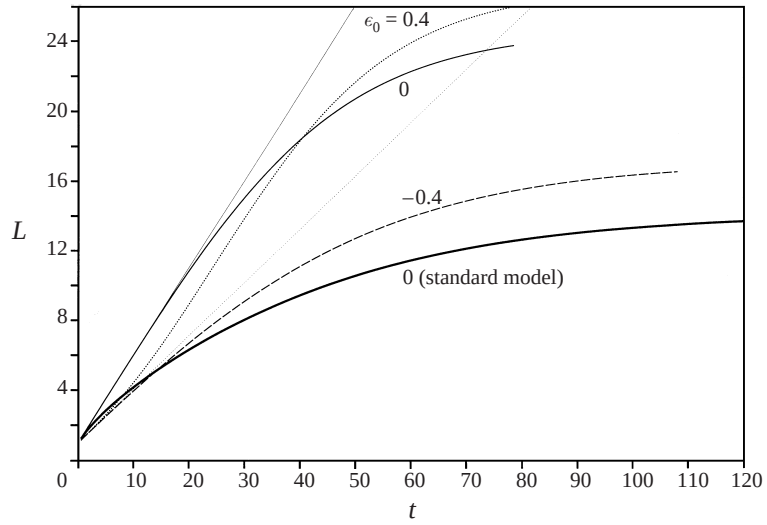


FIGURE 7. Intrusion length evolution as calculated from the integral model with a constant nose height $h$, with different values of $\varepsilon_0$ ($\tau_v/\tau_s = 0.0042, \alpha = 0, Fr = 1$). The thin straight lines are for $\alpha = 1$. For comparison, the solution of the standard model at the same parameter values is also shown.

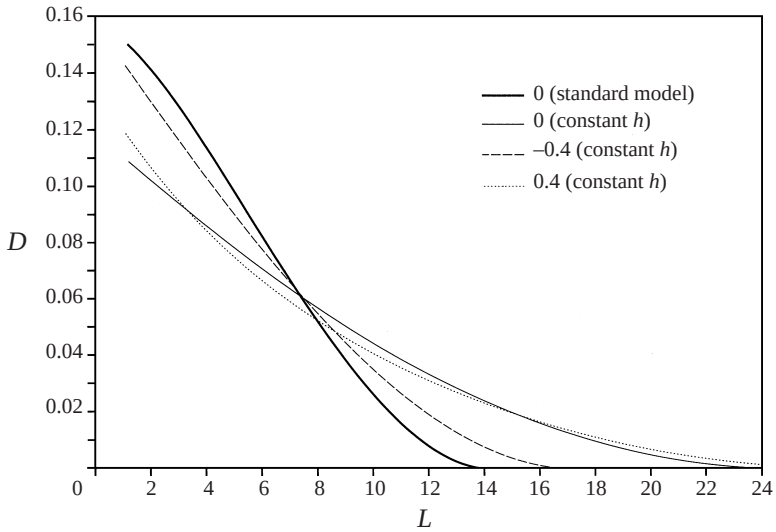


FIGURE 8. Sediment distribution as calculated from the integral model with a constant nose height $h$, at different values of $\varepsilon_0$ ($\tau_v/\tau_s = 0.0042,\ \alpha = 0,\ Fr = 1$). The solution of the standard model is shown for comparison.

are very similar to the ones shown in figure 6 for the varying propagation speed integral model: the extent of the deposit from the initially light intrusion ($\varepsilon_0 = -0.4$) is relatively short, but the deposit extent from the symmetric and the dense intrusion are very similar. The constant nose height in this model yields, for all values of $\varepsilon_0$, a slightly longer deposit extent than the standard integral model.

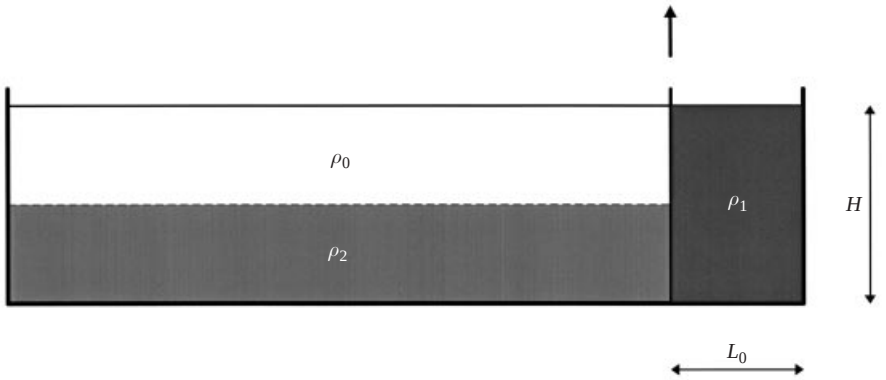


FIGURE 9. Sketch of the experimental arrangement. Most experiments were performed in a tank with a total length of 200 cm, $L_0 = 10$ cm and $H = 20$ cm.

| | Experiment | $\varepsilon_0$ | |
|---|---|---|---|
| Saline intrusions | exp. 2 | 0.20 | |
| | exp. 4 | −0.27 | |
| | exp. 9 | 0.02 | |
| Particulate intrusions | exp. 1 | −0.11 | |
| | exp. 3 | 0.11 | |
| | exp. 10 | −0.31 | |
| | exp. 12 | −0.23 | |
| | exp. 18 | 0.32 | (long tank) |
| | exp. 20 | 0.35 | |
| | exp. 22 | 0.35 | (long tank) |
| | exp. 23 | 0.37 | (long tank) |

TABLE 1. Summary of the experiments described in the text.

## 3. Experimental arrangement

The majority of the experiments were conducted in a rectangular Perspex tank with internal dimensions $200 \times 20 \times 25\,\mathrm{cm}^3$ ($l \times b \times d$). A removable Perspex gate with foam seals around its edges was placed vertically in the tank at 10.0 cm from the endwall, as shown schematically in figure 9, to create two-dimensional lock releases.

In the first series of experiments, summarized in table 1, the long section of the tank in front of the gate was filled with two layers of fluid of equal depth. First, a 10.0 cm deep layer of salty water was put in the tank, and dyed green with food colouring. The density $\rho_2$ of this saline layer was measured with a digital refractometer to be approximately $1.02\,\mathrm{g\,cm^{-3}}$. Subsequently, the second, lighter layer was added by carefully pouring fresh water (density $\rho_0 = 1.00\,\mathrm{g\,cm^{-3}}$) on top of the first layer via a porous float. This gave a total fluid depth $H$ of 20.0 cm, and a reduced gravity $g'_{02}$ for the two-layer system of $20\,\mathrm{cm\,s^{-2}}$. The experiments were carried out no later than half an hour after filling the tank to reduce the effects of diffusion across the interface. The thickness of the interface between the two layers at the start of the experiments was observed by eye to be typically around 0.5 cm, but no accurate measurements are available.

In the experiments on saline intrusions, the section of the tank behind the gate, the lock, was filled with salty water of density $\rho_1$, dyed red with food colouring.

For the particle-driven intrusions the lock was filled with fresh water ($\rho_0$), to which a measured amount of silicon carbide particles was added to give the desired bulk density $\rho_1$ of the lock release. In some of the experiments, the interstitial fluid was dyed red in order to visualize the detrainment. The lock was vigorously stirred before the release to bring all the particles into suspension and to make the concentration uniform over the lock.

The particles, ordinarily used for industrial polishing, had a density $\rho_p$ of $3.217\,\mathrm{g\,cm^{-3}}$, and a size distribution with narrow peak around $d = 37\,\mu\mathrm{m}$. Assuming the particles are approximately spherical, this gives a Stokes settling velocity $V_s$ of $0.165\,\mathrm{cm\,s^{-1}}$. The Reynolds number of the settling particles is approximately $6 \times 10^{-2}$, clearly small enough for the Stokes approximation, used in the derivation of the settling velocity, to hold. However, the Reynolds number for the flow as a whole, based on the propagation velocity and depth of the intrusion was approximately $4 \times 10^3$. At these high Reynolds numbers, the role of viscosity in the flow evolution can be neglected and the analysis presented in § 2 can be applied.

The gravity intrusion was released by rapidly lifting the gate. The flow was recorded with a colour video camera, mounted on a tripod 4 m from the tank. The camera was panned to follow the intrusion as it propagated along the length of the channel.

A small number of experiments were carried out in a much larger tank, with inside dimensions $960 \times 26 \times 54\,\mathrm{cm^3}$. This tank was filled to a level of 25 cm, and releases were studied for a 40 cm long lock with a suspension of particles with diameter $d = 23\,\mu\mathrm{m}$. In these experiments the flow was recorded with a camera that was moved along the tank on a traversing mechanism to reduce the parallax experienced when the camera was panned. These experiments are marked 'long tank' in table 1.

The position of the nose of the intrusion was measured from the video recordings of the experiment using the DigImage system. The measurements were taken with respect to tick marks on the front of the tank, thus excluding parallax effects. From these data the propagation speed was calculated over 1 s time intervals. In the long tank experiments, a different technique was used: the time was logged when the intrusion crossed a tick mark, at 10 cm spacing on the back wall of the tank, and the velocity was calculated from those data. In the particle-driven experiments the sediment deposited on the bottom of the tank was siphoned up from several strips, 2.4 cm wide and stretching the full width of the tank. After decanting and boiling off the fluid, the weight of the sediment, and hence values of $D(x)$, was determined with a digital scale.

## 4. Experimental results

### 4.1. *Saline interfacial intrusions*

In the first series of experiments, saline gravity intrusions of various relative densities into a two-layer fluid are investigated. The first experiment to be described (exp. 9) was similar to those described by Britter & Simpson (1981): the lock was filled with saline fluid of a density that was equal to the average density of the top and bottom layer in front of the lock, corresponding to $\varepsilon = 0$ in (15). On removal of the gate this intermediate density fluid collapses symmetrically towards the horizontal midplane. All fluid from the lock is swept up into a wedge-shaped intrusion in this initial collapse phase. Return flows of light fluid along the surface and dense fluid along the bottom are observed. In the following description we will non-dimensionalize times and lengths with the propagation timescale $\tau_v$ (26) and the lock length $L_0$, respectively, as outlined in § 2.2.

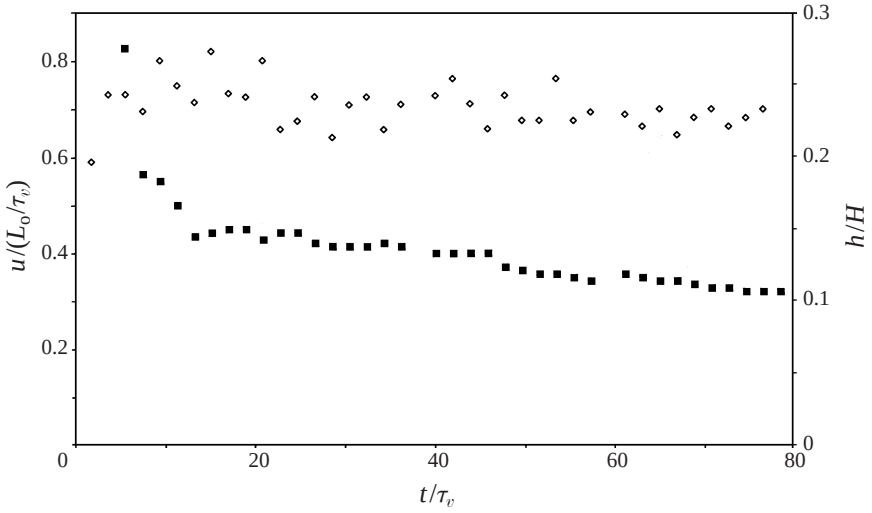


FIGURE 10. ◇, Propagation velocity and ■, nose thickness of a symmetric saline interfacial intrusion. Exp. 9, $\varepsilon = 0.02$.

Shortly after the release, the intrusion attains a state where its thickness does not vary along its length. The head of the intrusion maintains this approximately constant thickness, propagating along the interface at a constant velocity, until $t/\tau_v \approx 45$ (see figure 10). The intrusion has then reached a length of approximately 11 lock-lengths. During this phase of the development, the rounded nose of the intrusion stays quite symmetrical with respect to the interface ahead of it. The increased elevation of the nose $\zeta$ predicted by (2) is typically $10^{-4}$ m, too small to be observed in our experiments. The intrusion does not generate strong interfacial waves, and remains almost two-dimensional: only minor variations over the width of the tank are seen.

During this constant-head-thickness phase, the tail of the intrusion slowly thins as it lengthens. We did not observe the hydraulic jump that was reported for boundary gravity currents to propagate along the current towards the nose. Such a jump can be formed as a result of the reflection of the return flow off the tank endwall. The absence of this jump is probably due to the high aspect ratio of our lock: $h_0/x_0 = 2$. The experimental data indicate a decreasing thickness and a reducing propagation velocity after the intrusion propagated a distance of some 10 lock-lengths. This may be interpreted as the transition to the self-similar phase. The short length of our experimental tank, and also the high aspect ratio of our lock, do not make the present experimental set-up particularly suitable for investigating the evolution in this phase, and we will not consider it further here.

Next, we describe the case of a dense intrusion, with $\varepsilon > 0$. Figure 11 shows the time-evolution of a typical example (exp. 2). The flow does not evolve symmetrically after lifting the gate: the upper half of the lock release collapses much faster than the lower half and the corresponding return flow along the top is stronger. The intrusion propagates mainly in the dense bottom layer and pushes the dense layer somewhat ahead. The nose of the intrusion is just below the interface, rather than centred on it, although the interface between the two layers is raised just in front of the nose, a feature consistent with the raised stagnation point discussed in § 2.1. This asymmetry generates an interfacial wave ahead of the intrusion not seen in the experiments with an intrusion of average density ($\varepsilon = 0$). For this experiment, the amplitude and wavelength of this wave are approximately 4 cm and 1 cm, respectively.

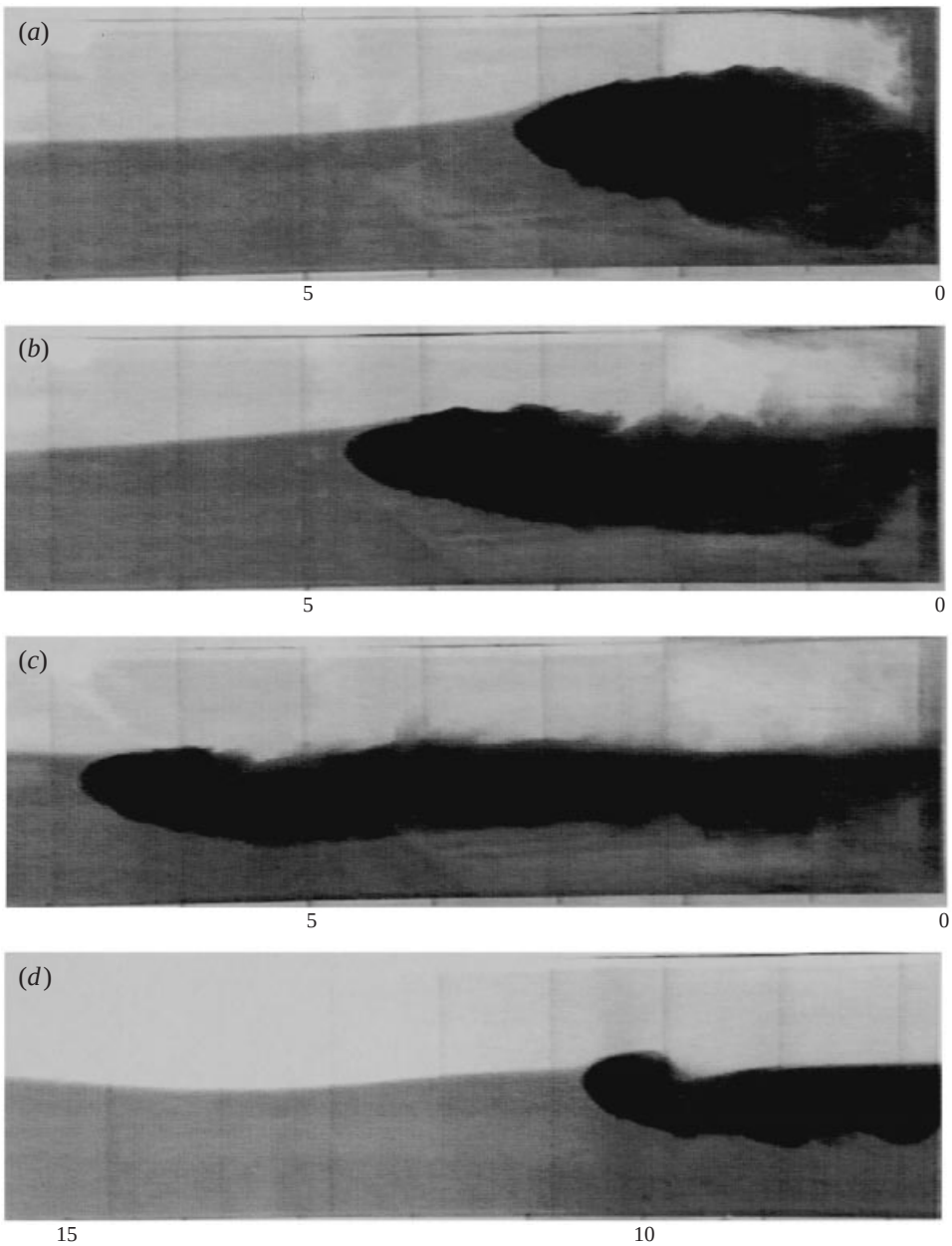


FIGURE 11. A series of images of a relatively dense saline interfacial intrusion, at $t/\tau_v = 9, 15, 25$ and 50 (Exp. 2, $\varepsilon = 0.20$). Length along the tank is indicated in non-dimensional units $x/L_0$. Note that, in the last frame, a different position along the tank is shown as the camera is panned with the nose of the intrusion.

After the collapse phase the intrusion propagates at a constant speed and with a constant head thickness, although the intrusion is moved up and down by the crests and troughs of the waves on the interface between the two ambient layers. This can be seen from the positions of the top and bottom of the head, plotted as a function of time in figure 12(*a*). This figure also shows that the mean position of the intrusion remains below the interface.

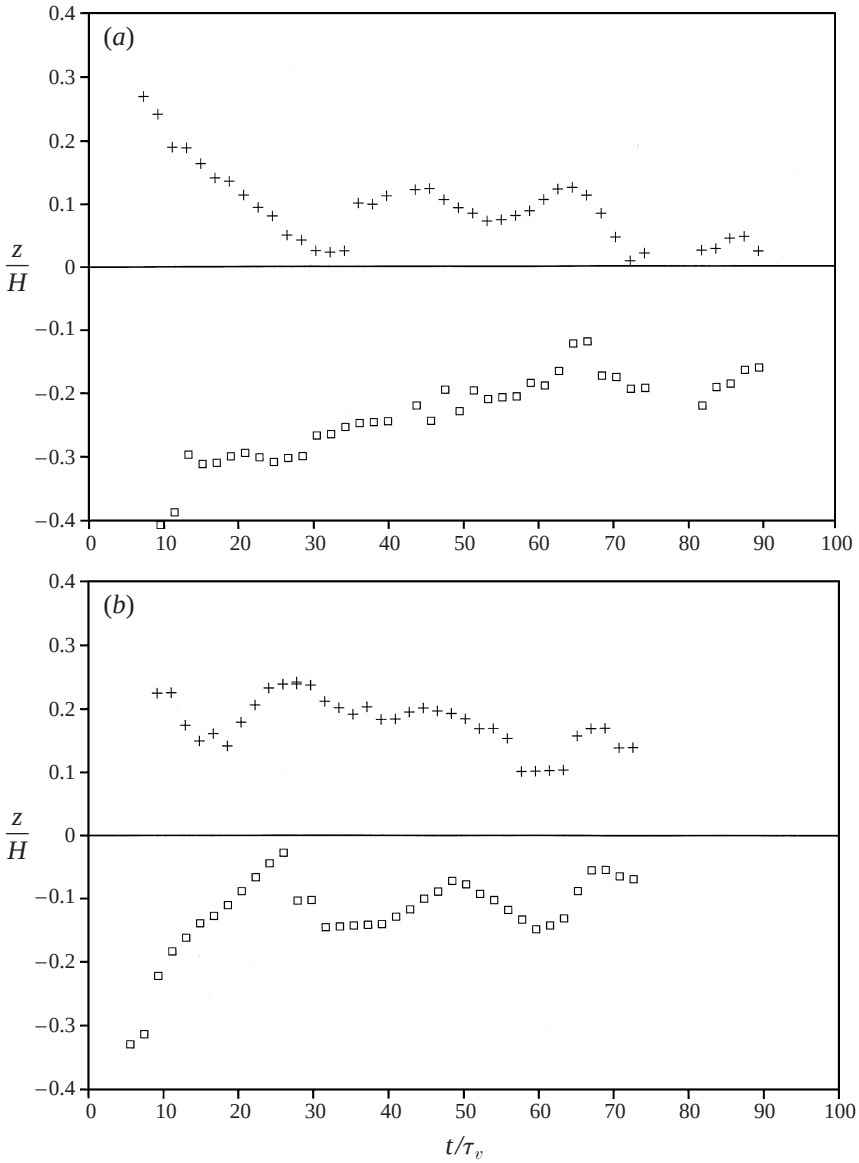


FIGURE 12. Position of +, the top and □, bottom of the nose of saline interfacial intrusions as a function of time. (*a*) Relatively dense intrusion: exp. 2, $\varepsilon = 0.20$. (*b*) Relatively light intrusion: exp. 4, $\varepsilon = -0.27$.

As with the symmetric intrusion no clear hydraulic jump occurs, but waves can be seen to travel on both interfaces of the intrusion towards the nose. These waves have a wavelength of approximately 40 cm, and are most pronounced on the upper interface, where the density jump is largest. Some turbulence and mixing is observed at both interfaces, but the effect on the mean density of the intrusion appears to be small. At approximately 10 lock lengths the intrusion begins to become thinner and to slow down.

Finally, we consider the light saline lock-release ($\varepsilon < 0$) of experiment exp. 4. The evolution is similar to the dense intrusion (exp. 2), but now inverted with respect to the

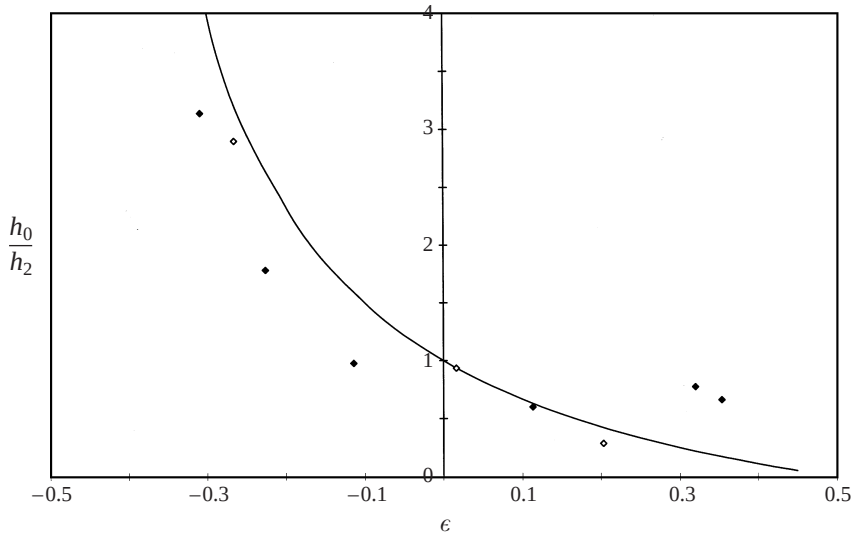


FIGURE 13. Ratio of intrusion heights in top and bottom layers against relative density parameter $\varepsilon$: ◇, saline intrusions; ◆, particle-driven intrusions.

interface. The intrusion propagates mainly in the lighter upper layer, pushing down the interface ahead of the nose. The asymmetry again generates interfacial waves that reflect off the endwalls of the experimental tank and interact with the intrusion. This can be seen quite clearly in the time-evolution of top and bottom heights in figure 12(*b*). This figure also suggests that the intrusion actually becomes more symmetrical as time progresses, possibly owing to the entrainment of fluid from the lower layer. The waves on the bottom interface of the intrusion have a larger amplitude than those on the top interface, which might indicate a larger amount of mixing there.

The open markers in figure 13 show the ratio $h_0/h_2$ of the intrusion thicknesses in the top and bottom layers, as a function of $\varepsilon$. These thicknesses were obtained by averaging over the time interval $20 \leqslant t/\tau_v \leqslant 30$, and the original, undisturbed height of the interface was taken as reference. The graph shows an excellent agreement between the experimental data and the prediction from (13) and (14), plotted as a solid curve.

All three intrusions were observed to propagate initially at an approximately constant speed. The initial propagation velocities of these saline intrusions are indicated as a function of the density parameter $\varepsilon$ by the open circles in figure 14. The values are non-dimensionalized with the measured intrusion thickness $h$ and ambient reduced gravity $g'_{02}$. The curve shows the intrusion velocity from (18), with the Froude number set to unity, as is appropriate for the ambient depth used in these experiments. The data display considerable scatter, and the theory cannot be validated quantitatively on the basis of these data. The thickness of the interface can have a sizeable effect on the propagation velocity of the intrusion. Unfortunately, this effect could not be corrected for, as the thickness was not measured. Also, the range of $\varepsilon$-values could not be extended, since $-0.5 \leqslant \varepsilon \leqslant +0.5$ and at the limiting values the density difference with one of the layers will be zero and no intrusion forms.

### 4.2. *Particle-driven interfacial intrusions*

We now turn our attention to intrusions of a particle-laden fluid into a two-layer stratification. For all initial particle concentrations $\phi_0$, we found that almost all

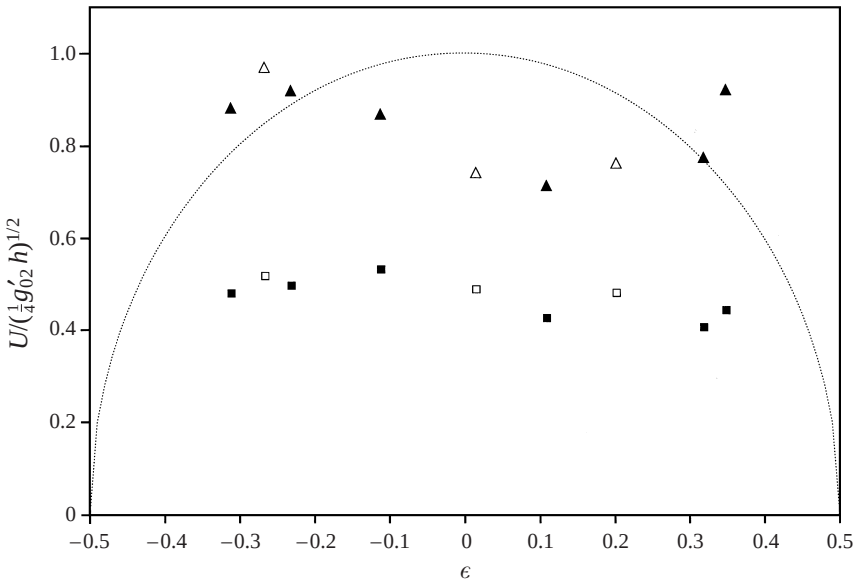


FIGURE 14. Intrusion propagation velocity against relative density parameter $\varepsilon$. The velocities are non-dimensionalized with the ambient reduced gravity, and with the measured initial intrusion thickness $h$ for triangles and the ambient depth $H$ for squares. △, saline intrusions; ▲, particle-driven intrusions. The curve represents the prediction from equation (18) with $Fr = 1$.

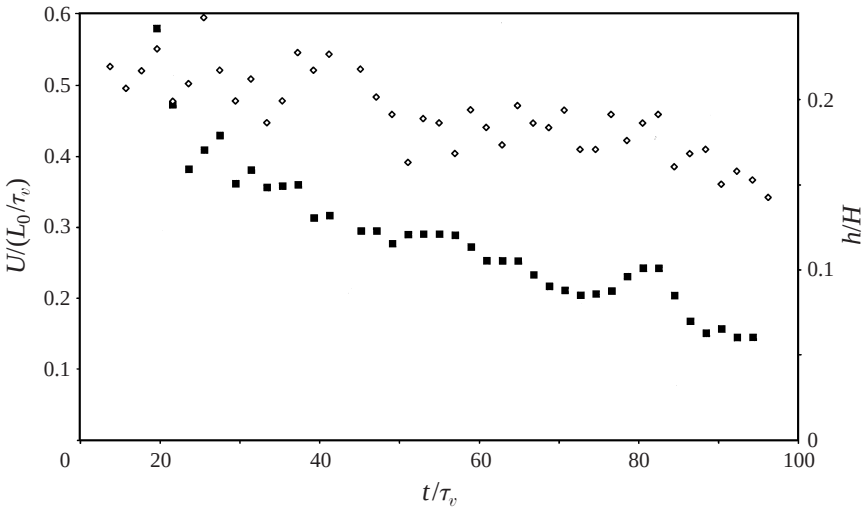


FIGURE 15. ◇, propagation velocity and ■, nose thickness of an approximately symmetric particle-driven interfacial intrusion. Exp. 3, $\varepsilon_0 = 0.11$.

particles become swept up into the intrusion immediately after the release, and so the bulk density of the lock-release suspension $\rho_1 = \rho_i + \phi(\rho_p - \rho_i)$ was used to calculate the relative density parameter $\varepsilon_0$ from (15). We only consider intrusions that are driven purely by the suspended particles: the density of the interstitial fluid is equal to the density of the top layer: $\rho_i = \rho_0$. Intrusions driven by the buoyancy of the interstitial fluid were described in the preceding section, but we have not yet investigated intrusions with a combined driving force.

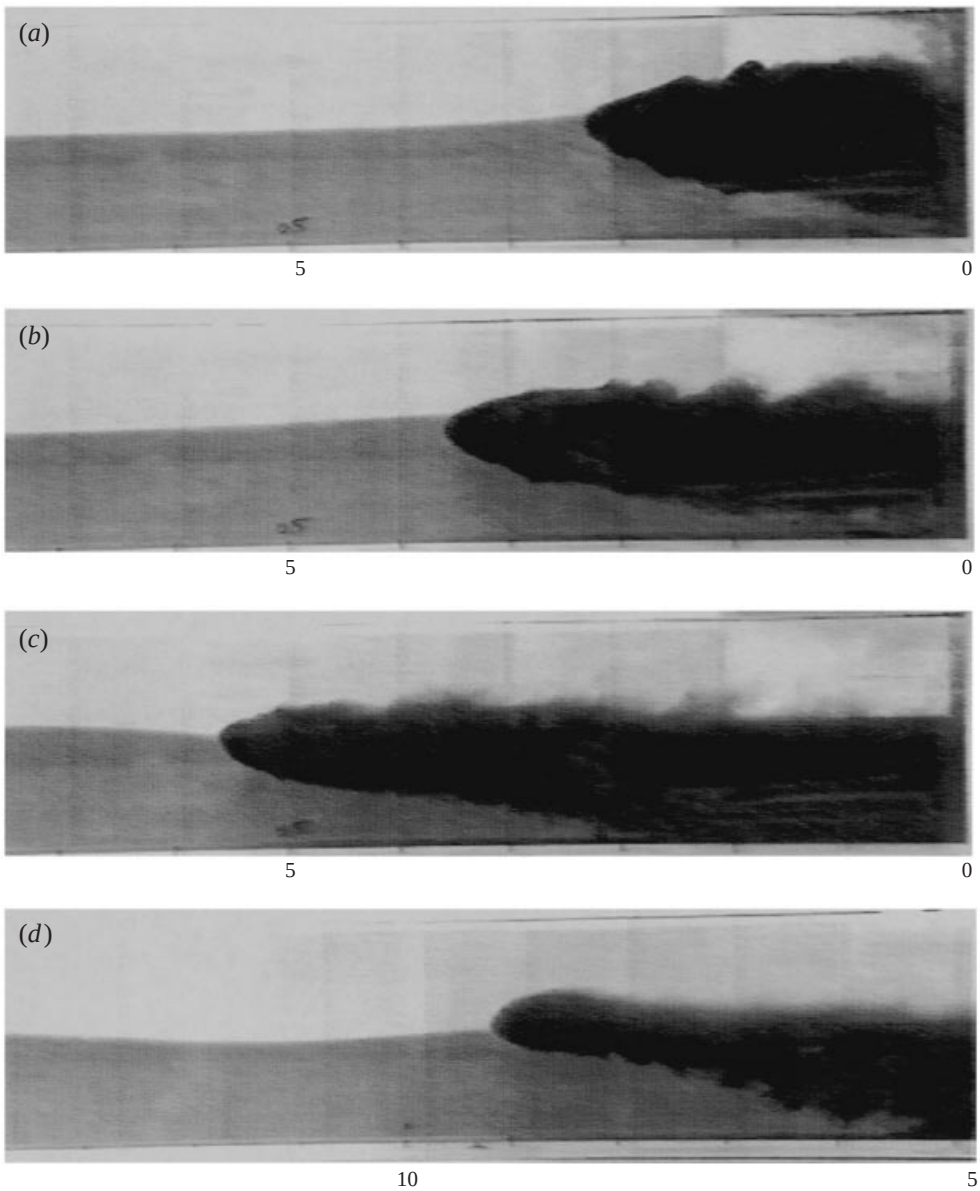


FIGURE 16. A series of images of an initially relatively dense particle-driven interfacial intrusion, at $t/\tau_v = 9, 15, 25$ and 42. Exp. 3, $\varepsilon_0 = 0.11$. Length along the tank is indicated in non-dimensional units $x/L_0$. Note that different positions along the tank are shown as the camera is panned with the nose of the intrusion.

In the initial collapse phase, the particle-driven intrusions evolve in the same way as saline intrusions with equal value of $\varepsilon$. In the subsequent phase, starting at $t/\tau_v \approx 20$, corresponding to about 5 lock lengths, the particle-driven intrusions deviate from the saline intrusions. The thickness of the head of the intrusion does not remain constant, as was shown in figure 10 for a saline intrusion, but decreases slowly as shown in figure 15 for a symmetrical particle-driven intrusion. The graph also indicates that the propagation velocity slowly decreases with time.

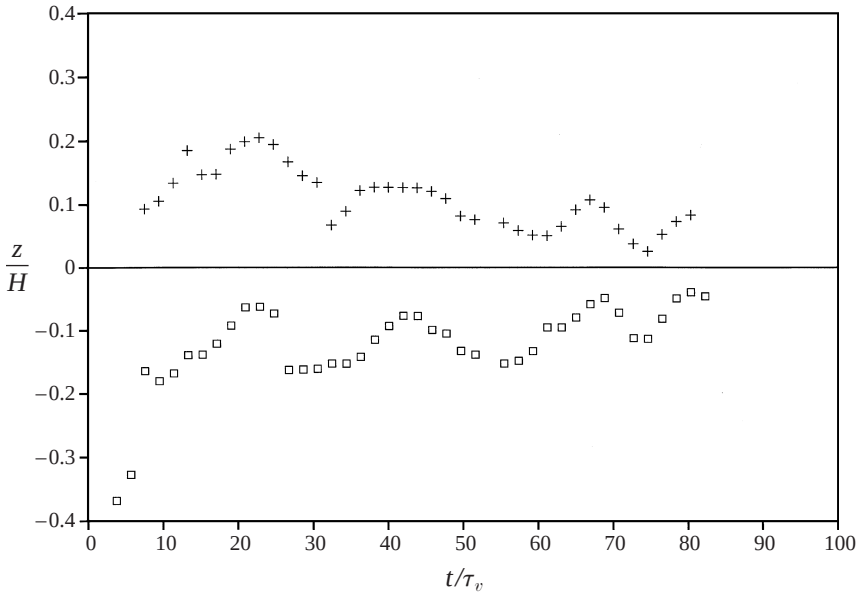


FIGURE 17. Position of +, the top and □, bottom of the nose of a relatively light, particle-driven intrusion as a function of time. Exp. 12, $\varepsilon_0 = -0.23$.

The flow of a typical dense particle-driven intrusion ($\varepsilon_0 > 0$) is shown in figure 16. After the asymmetric collapse, the intrusion propagates mainly in the dense layer, with its nose just below the interface. As for the asymmetric saline intrusions ($\varepsilon \neq 0$; see figure 11 for comparison), this generates strong interfacial waves. Very soon after the collapse the particles begin to settle out of the intrusion, the settling occurring over almost its entire length. Over the first 15 cm behind the nose of the intrusion, the sedimenting particles travel only a very small vertical distance. Further behind the nose, the sedimentation speed is apparently enhanced by the convection, which arises from the statically unstable bottom-layer fluid containing particles overlying fluid without particles. The particles settle to the floor of the tank, and are swept back by the mean return flow in the bottom layer. There is some detrainment of interstitial fluid at the top, but the rest of the body of the intrusion seems to be well-mixed at all times. The concentration of particles decreases, which reduces the density difference between the intrusion and the top layer, and causes the intrusion to rise. The nose that was initially below the interface, first becomes centred on it and is raised above it at larger stages.

As the intrusion propagates, both the head and tail become thinner. After $t/\tau_v \approx 75$ the head contains almost no particles. However, the intrusion, which is only 2 cm thick by this time, is still propagating forwards. This is most probably due to the earlier entrainment of some dense fluid from the lower layer into the intrusion, giving it an intermediate density. Entrainment of upper-layer fluid will not, by itself, provide the density contrast to drive the intrusion, but will instead reduce the effect of fluid entrained from the lower layer. The observation that the initially colourless interstitial fluid of the intrusion has become green in the final phase indicates that it has entrained dense (green) fluid.

In the experiments with lighter particle-driven intrusions ($\varepsilon_0 < 0$) the sedimentation of particles from the intrusion does not appear to start until $t/\tau_v \approx 30$. This may be

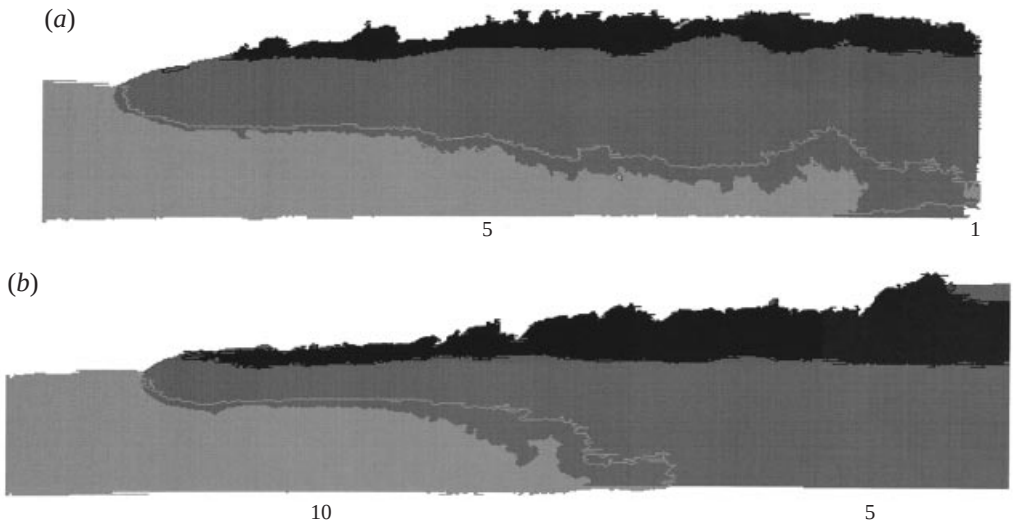


FIGURE 18. Images showing the detrainment at (*a*) $t/\tau_v = 30$ and (*b*) 50 after release of a particle-driven intrusion into a two-layer stratification. The ambient layers are coloured white and light grey. The dark grey bottom part of the intrusion contains both particles and interstitial fluid, but the black area at the top contains almost all interstitial fluid. Exp. 12, $\varepsilon_0 = -0.23$. Horizontal distance from the back of the lock is indicated in non-dimensional units $x/L_0$.

due to the stronger return flow in the lower layer and the upward movement of the lock fluid as a whole, masking any downward settling of particles. The graph of the top and bottom heights in figure 17 shows that the light intrusion (exp. 12) collapses asymmetrically, like the saline equivalent. The head is mainly above the interface at the end of the collapse phase. Surprisingly enough, the head then sinks to become centred on the interface, although still moving up and down owing to the interfacial waves. This could be an effect of entrainment of dense fluid from the lower layer into the head of the intrusion, as also remarked for saline intrusions. Detrainment of interstitial fluid before the sedimentation of particles starts, thereby increasing the particle concentration, could also play a role. Figure 18 shows the detrainment of interstitial fluid from the intrusion, at $t/\tau_v = 30$ and 50. These images were obtained by combining the information of the separate colour channels of the video recordings. The black area at the top of the intrusion represents detrained interstitial fluid with only very few particles. However, the sharp border between the intrusion and the detrained fluid is an artefact of the analysis procedure: all parts of the intrusion with a particle concentration below a certain threshold were coloured black in this image.

The theoretical prediction for the ratio of the thicknesses of the intrusion in the top and bottom layer matches the data quite well over most of the range of $\varepsilon_0$, as can be seen from the solid markers in figure 13. For very dense intrusions ($\varepsilon_0 > 0.2$), the observed ratio is significantly higher than the theory predicts. These intrusions penetrate relatively deeply into the upper layer, perhaps caused by an early loss of particles from these dense suspensions in the collapse phase.

For the first 10 s after release, the intrusions travel at an approximately constant speed. In this collapse phase there is no distinction between particle-driven and saline intrusions. The speed then starts decreasing and the particle-driven intrusions propagate slower than their saline counterparts. The non-dimensionalized initial propagation velocities are indicated by the solid circles of figure 14. This graph shows

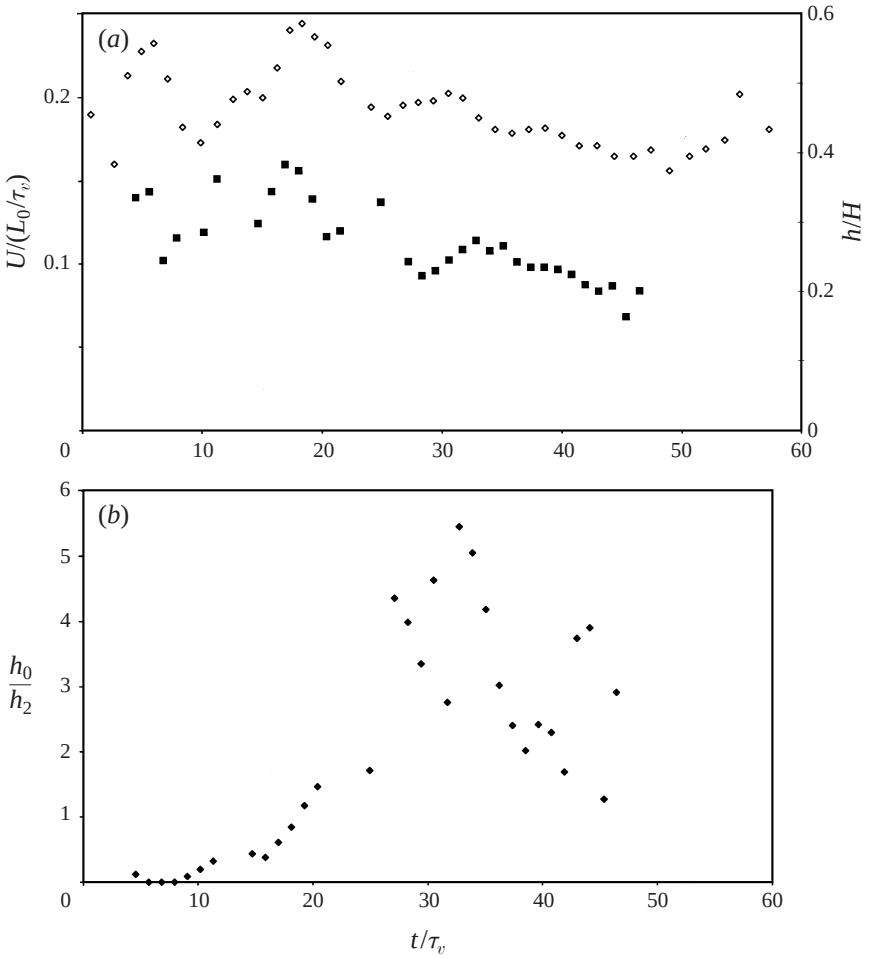


FIGURE 19. Time-evolution of a particle-driven intrusion in the long tank. Exp. 18, $\varepsilon_0 = 0.32$. (*a*) ◇, Propagation velocity and ■, nose thickness; (*b*) the ratio of intrusion height in top and bottom layer.

a disappointing amount of scatter and no noticeable dependence on the density parameter $\varepsilon$ . The theoretically predicted dependency could not be verified because of the reason mentioned above: the thickness of the interface affects the velocity relatively strongly.

In an attempt to verify the theoretical predictions for the velocity as a function of the density parameter $\varepsilon$ at a constant interface thickness, a number of experiments with very dense particle-driven intrusions were carried out in a much longer tank (see table 1). A correspondingly longer lock was used, with a suspension of smaller particles, in order to create an intrusion that would not thin too quickly. Figure 19(*a*) shows that the thickness of the intrusion fluctuates between $0.25H$ and $0.4H$, but the thickness does not start to decrease systematically until $t/\tau_v \approx 25$. Figure 19(*a*) also shows that the velocity fluctuates somewhat in the collapse phase, which lasts up to $t/\tau_v \approx 10$ or 3 lock lengths after the release in this experiment. During the period $10 \leqslant t/\tau_v \leqslant 25$ the velocity increases to a maximum at around $t/\tau_v = 18$, and then decreases. Since the particles are sedimenting out of the intrusion and thereby

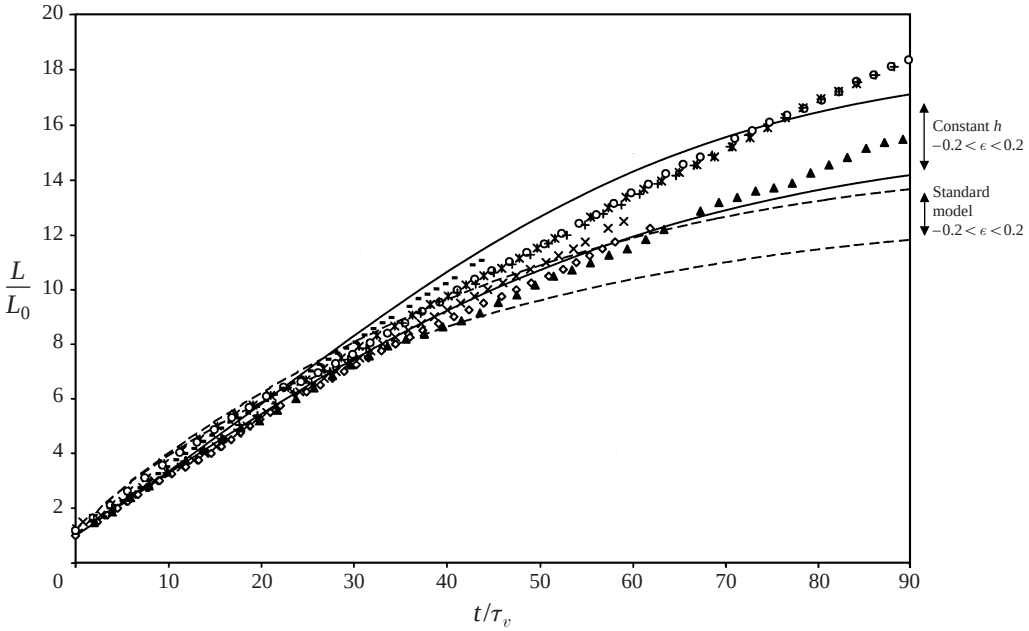


FIGURE 20. Non-dimensionalized intrusion length versus time. Symbols represent all experimental measurements. Dashed curves are solutions of the integral model for different values of $\varepsilon_0$. ($\alpha = 0, Fr = 1; \tau_v/\tau_s$ from experimental conditions). Solid curves show solutions of the model with a constant nose height.

continuously reducing $\varepsilon$, the increase and subsequent decrease in velocity conforms with the predictions of (18). The timing of the velocity maximum is consistent with the visual observation that the nose of the intrusion rose from below the interface to above the interface, being centred at the interface between $t/\tau_v \approx 17$ and 19. The time-evolution of the ratio $h_0/h_2$ in figure 19($b$) also confirms the theory: it starts at values close to zero (intrusion mainly in lower layer), reaches unity at $t/\tau_v \approx 18$ (intrusion symmetrical) and increases to larger values at later times (intrusion mainly in upper layer).

The lengths of the particle-driven intrusions are shown in figure 20. The curves plotted on the graph are the solutions of our integral model, where we have set the detrainment parameter $\alpha = 0$ and the Froude number to 1, which, according to Britter & Simpson (1981), is appropriate for the ambient depth in our experiments. The dashed curves are solutions of the integral model, for both the upper and lower $\varepsilon$ values in our experiments. The curves match the experimental observations very well at early times, but can be seen to underpredict the length at later times. The solid curves are the solutions for the integral model with the nose height $h$ kept constant, again for the upper and lower end of the experimental range for the relative density parameter $\varepsilon_0$. These show better match with the experiments at later times. Towards the end of the experiments, especially in the long tank, mixing with fluid from top and bottom layers makes it a salinity-driven rather than particle-driven intrusion, and the model developed in this paper no longer applies.

To look in more detail at the propagation velocity, the velocities of two similar intrusions in the long tank are plotted against time in figure 21. The initial velocity fluctuations, up to non-dimensional time $t/\tau_v = 10$, seem to be systematic, and

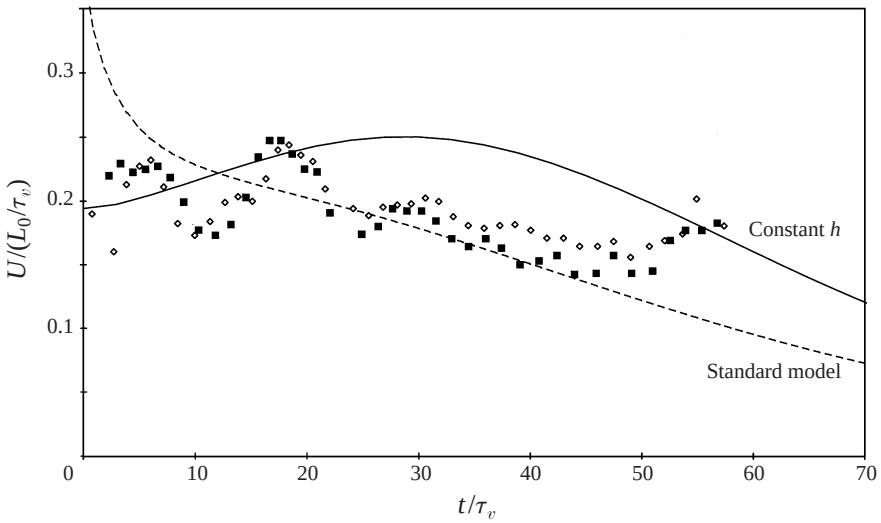


FIGURE 21. Propagation velocity versus time. The symbols represent experimental data from exp. 18 and exp. 22, the dashed curve is the solution of the integral model, and the solid curve is the solutions of the integral model with a constant nose height ($\alpha = 0$, $Fr = 1$; $\varepsilon_0$ and $\tau_v/\tau_s$ from experimental conditions).

are thought to be a result of the particular release conditions in our experimental arrangement and the waves on the free surface they produce. Subsequently, the velocity is observed to reach a maximum, as was previously pointed out in figure 19(*a*). This maximum was observed in all interfacial intrusion experiments with an initial relatively dense intrusion ($\varepsilon_0 > 0$). The dashed line, showing the solution of the integral model at these particular experimental parameters, predicts the magnitude of the velocity quite well. It does not exhibit a velocity maximum: the propagation velocity reduces too quickly owing to the thinning of the intrusion. The solid line, showing the solution of the model with a constant nose height, does indicate a maximum in the velocity at the point where the intrusion has become symmetric with respect to the interface. However, the time at which the maximum is reached in the experiment is much earlier than the model predicts. This indicates that future models will have to include both a constant nose height at early times (corresponding to the slumping phase) and a decreasing nose height at later times (the similarity phase) to model these particle-driven intrusions more accurately. Nevertheless the present models already provide satisfactory predictions.

Figure 22 shows the distribution of deposited particles along the length of the tank, measured after the intrusion has terminated. The figures are based on the same data, but different scalings are applied. The results of three experiments are plotted: a dense intrusion (exp. 3, $\varepsilon_0 = 0.11$), a light intrusion (exp. 1, $\varepsilon_0 = -0.11$), and a very light intrusion (exp. 10, $\varepsilon_0 = -0.31$). Integrated over the length of the tank these discrete deposition distributions give total deposits that are within 5% of the actual total particle mass in the lock-release. This suggests that the method for measuring the deposit is accurate to within approximately $5\sqrt{n} = 20\%$ for each of the $n$ individual point measurements.

Because of the return flow in the lower layer under the intrusion, we expect the sedimenting particles to be swept back towards the lock before they settle on the tank floor. This effects is indeed observed if we compare our experimental

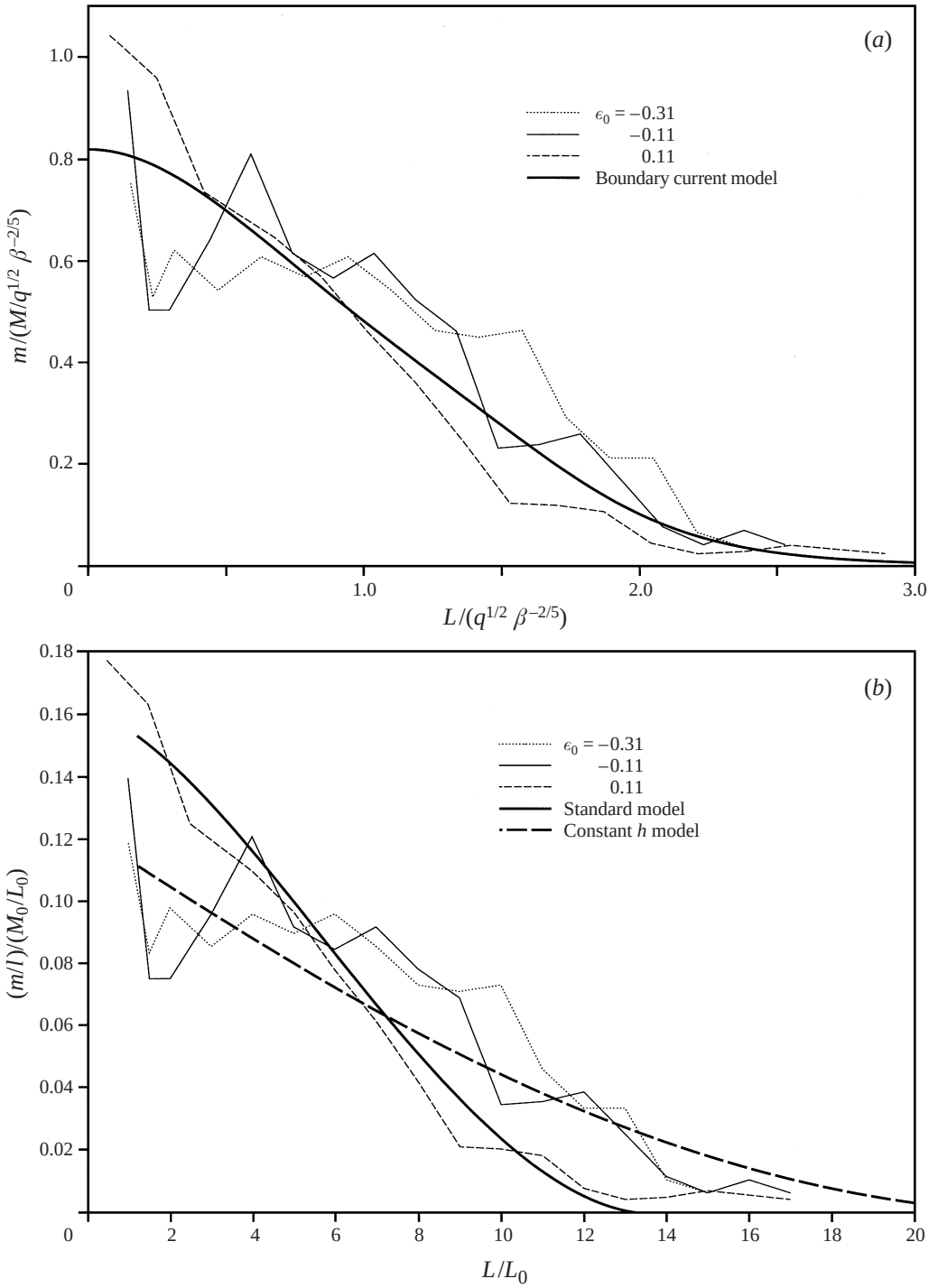


FIGURE 22. Final sediment distribution data from three experiments, with different values of $\varepsilon_0$. (*a*) Data scaled as in Bonnecaze *et al.* (1996). The thick solid curve shows their numerical solution for a particle-driven current along the a boundary, with parameters as described in the text. (*b*) Data scaled with the initial conditions. The thick solid curve is the solution of the standard integral intrusion model, the thick dashed curve is the solution of the constant-$h$ model ($Fr = 1, \alpha = 0, \varepsilon_0 = -0.11$).

measurements for an intrusion with the experimental data for a boundary current presented by Bonnecaze *et al.* (1996): they measured a maximum in the deposit at some distance away from the lock, whereas our deposition distribution follows an almost monotonically decreasing curve.

Figure 22(*a*) compares our experimental results with the model suggested by Bonnecaze *et al.* (1996) for particle-driven currents along a rigid boundary. The data are non-dimensionalized with scales based on the initial volume per unit breadth $q = x_0 h_0$ and the settling parameter $\beta$. The latter is defined as $V_s/U$, with an intrusion velocity scale $U$ from (18) without the $\varepsilon$-dependence, and an intrusion height $h = q^{1/2}$. The curve shown is the algebraic approximation to the numerical solution of the shallow-water equations, giving the particle deposit per unit length along the tank, in dimensional and non-dimensional form:

$$\left.\begin{aligned} w(x) &= Mq^{-1/2}\beta^{2/5} W(xq^{-1/2}\beta^{2/5}), \\ W(x^*) &= 0.820/(1 + 0.683x^{*2} + 0.017x^{*8}). \end{aligned}\right\} \tag{46}$$

Here, $M$ represents the total mass of particles. This model matches the data of these intrusion experiments surprisingly well, although we have simply put the intrusion propagation velocity, that we derived in § 2.1, into the model for a boundary current. This indicates that the driving bulk buoyancy of the current or intrusion, combined with the particle sedimentation velocity, largely determines the deposition distribution.

Figure 22(*b*) shows the same deposition measurements, but now scaled following the non-dimensionalization described in § 2.2. Both the numerical solution of our standard integral model for an interfacial intrusion and the solution of our constant-$h$ model are shown on the graph. The standard model predicts a run-out length that is slightly too short, as already pointed out in the discussion of figure 20, and future models would have to include some characteristics of the constant-$h$ model. However, these simple integral models already yield a good agreement with the experimental data.

## 5. Conclusions

Saline intrusions along the interface in a two-layer stratification propagate at a constant velocity shortly after the release, just like gravity currents along a rigid boundary. The experimentally observed propagation velocity is well predicted by the theory based on balancing the inertial and buoyancy forces. Predictions of the relative heights of the intrusion in the two layers are also in close agreement with the experiments. The interfacial waves generated by the intrusion were observed to be weaker for more symmetrical intrusions. The present experimental tank was too short to verify the predictions for the propagation speed in the self-similar phase.

Intrusions along an interface driven by suspended particles were seen to follow the same behaviour as saline intrusions in the initial phase, collapsing towards the interface and then propagating away from the lock at a constant speed. As particles settle out, the particle-driven intrusions deviate from the saline intrusions and gradually slow down. The propagation velocity depends strongly on the interface thickness, complicating verification of the predictions of the propagation velocity. An experiment in a very long tank, however, showed that the prediction for the velocity as a function of the relative density matches reasonably well, with the maximum velocity occurring when the intrusion is symmetrical. The prediction for relative intrusion heights are again in close agreement with the measurements.

Experiments with a dyed interstitial fluid were performed to visualize the detrainment of interstitial fluid which turned out to be substantial. A simple integral model for particle-driven interfacial intrusions has been developed, which includes the effects of detrainment and sedimentation. The model predicts the early time-evolution of the length of intrusions accurately. The match with experimental data at intermediate times is further increased by assuming a constant intrusion nose height during the slumping phase. During the very late phases of the flow, entrainment of ambient fluid into the head of the intrusion also plays a major role. This provides the intrusion with a driving buoyancy difference after all the particles have settled out, and the simple model no longer applies.

The deposition of sediment on the floor of the tank is well predicted by the simple integral model for interfacial intrusions. The shallow-layer model for currents along a rigid boundary described by Bonnecaze *et al.* (1996) also matches the experimental data for these intrusions.

The support for this project from Yorkshire Water is gratefully acknowledged.

## REFERENCES

Benjamin, T. B. 1968 Gravity currents and related phenomena. *J. Fluid Mech.* **31**, 209–248.

Bonnecaze, R. T., Hallworth, M. A., Huppert, H. E. & Lister, J. R. 1995 Axisymmetric particle-driven gravity currents. *J. Fluid Mech.* **294**, 93–121.

Bonnecaze, R. T., Huppert, H. E. & Lister, J. R. 1993 Particle-driven gravity currents. *J. Fluid Mech.* **250**, 339–369.

Bonnecaze, R. T., Huppert, H. E. & Lister, J. R. 1996 Patterns of sedimentation from polydisperse turbidity currents. *Proc. R. Soc. Lond.* A **452**, 2247–2261.

Britter, R. E. & Simpson, J. E. 1981 A note on the structure of an intrusive gravity current. *J. Fluid Mech.* **112**, 459–466.

Dade, W. B. & Huppert, H. E. 1995 Runout and fine-sediment deposits of axisymmetric turbidity currents. *J. Geophys. Res.* **100**, 18597–18609.

Holyer, J. Y. & Huppert, H. E. 1980 Gravity currents entering a two-layer fluid. *J. Fluid Mech.* **100**, 739–767.

Huppert, H. E. & Simpson, J. E. 1980 The slumping of gravity currents. *J. Fluid Mech.* **99**, 785–799.

Maxworthy, T. 1999 The dynamics of sedimenting surface gravity currents. In preparation.

Rimoldi, B., Alexander, J. & Morris, S. 1996 Experimental turbidity currents entering density-stratified water: analogues for turbidities in Mediterranean hypersaline basins. *Sedimentology* **43**, 527–540.

Rottman, J. W. & Simpson, J. E. 1989 The formation of internal bores in the atmosphere: a laboratory model. *Q. J. R. Met. Soc.* **115**, 941–963.

Simpson, J. E. 1997 *Gravity Currents in the Environment and the Laboratory*, 2nd edn. Cambridge University Press.